Journal of Nuclear Materials 581 (2023) 154422

Contents lists available at ScienceDirect

Journal of Nuclear Materials

journal homepage: www.elsevier.com/locate/jnucmat

# Ab initio study of tungsten-based alloys under fusion power-plant conditions

Yichen Qian[a], Mark R. Gilbert[b], Lucile Dezerald[c], Duc Nguyen-Manh[b], David Cereceda[a,*]

[a] Department of Mechanical Engineering, Villanova University, Villanova, PA 19085, USA
[b] United Kingdom Atomic Energy Authority, Culham Centre for Fusion Energy, Culham Science Centre, Abingdon, Oxon OX14 3DB, UK
[c] Institut Jean Lamour, CNRS UMR 7189, Universite de Lorraine, F-54000 Nancy, France

ARTICLE INFO

*Article history:*
Received 1 December 2022
Revised 29 March 2023
Accepted 31 March 2023
Available online 1 April 2023

*Keywords:*
Plasma-facing materials
Tungsten
Nuclear transmutation
First-principles calculations
Fusion

ABSTRACT

Tungsten (W) is considered a leading candidate for structural and functional materials in future fusion energy devices. The most attractive properties of tungsten for magnetic and inertial fusion energy reactors are its high melting point, high thermal conductivity, low sputtering yield, and low long-term disposal radioactive footprint. However, tungsten also presents a very low fracture toughness, primarily associated with inter-granular failure and bulk plasticity, limiting its applications. In recent years, several families of tungsten-based alloys have been explored to overcome the aforementioned limitations of pure tungsten. These include tungsten-based high-entropy alloys (W-HEAs) and tungsten-based Self-passivating Metal Alloys with Reduced Thermo-oxidation or "SMART alloys" (W-SAs). Given their proximity to the plasma, it is crucial to understand how the exposure of these candidate plasma-facing materials (PFMs) to the neutron fluxes expected in fusion reactors impacts their material behavior over time. In this work, we present a computational approach that combines inventory codes and first-principles DFT electronic structure calculations to understand the behavior of transmuting tungsten-based PFMs. In particular, we calculate the changes in the chemical composition, production uncertainties, the elastic and ductility properties, and the density of states for five tungsten-based PFMs when exposed to EU-DEMO fusion first wall conditions for ten years.



## 1. Introduction

Tungsten (W) is considered a leading candidate for plasma-facing applications in magnetic fusion energy (MFE) devices. The most attractive properties of W for MFE are its high melting point and thermal conductivity, low sputtering yield and low long-term disposal radioactive footprint. These advantages are accompanied unfortunately by very low fracture toughness characterized by brittle trans- and inter-granular failure, which severely restricts its operating temperature window [1].

In recent years, several families of W-based alloys have been explored to overcome the aforementioned limitations of pure W. High-entropy alloys (HEAs) are a promising class of materials with remarkable properties [2–5]. They were originally conceived in the early 2000s as a blend of five or more elements with individual concentrations between 5 and 35 atomic percent [6]. Interestingly, the composition stability of different HEA phases is strongly correlated with the valence electron concentration from electronic structure analysis [7]. In particular, tungsten-based HEAs (W-HEAs) have shown superior mechanical properties at high temperatures, a superior melting point (above 2873 K), enhanced radiation resistance to heavy ion irradiation, and negligible radiation hardening when compared to pure W [8–13]. Another attractive option are the so-called tungsten-based "SMART alloys" (W-SAs), where SMART stands for **S**elf-passivating **M**etal **A**lloys with **R**educed **T**hermo-oxidation, that can adapt their behavior to the environment [14–18]. For example, in the event of a loss-of-coolant accident (LOCA) combined with an air ingress, W-SAs containing small amounts of Ti or Y have demonstrated the capability to create stable oxides that prevent their mobilization into the atmosphere.

The exposure of W-based plasma-facing materials (PFMs) to high neutron fluxes causes nuclear reactions that can change the nuclide composition over time. The reactions lead to the production of radionuclides, causing a material to become activated,

* Corresponding author.
*E-mail address:* david.cereceda@villanova.edu (D. Cereceda).

https://doi.org/10.1016/j.jnucmat.2023.154422

while also producing nuclides of new elements, a process known as transmutation, that can alter material properties. Both activation and transmutation are commonly observed in fields such as nuclear fission, nuclear fusion, astrophysics, nuclear security, and medical research. Since activation can create hazard and transmutation can change material performance, it is vital to carefully understand the nuclear reaction rates. Inventory codes are frequently used to predict the response of materials to a specific neutron irradiation field. Such an approach consists of numerically solving a set of coupled differential equations that describe the rate of change of all possible nuclides and thus evolve the nuclide composition in time [19,20].

Experimentally, neutron irradiation campaigns at the fast test reactor Joyo [21–26], the Japan Materials Testing Reactor (JMTR) [25–27], and the High Flux Isotope Reactor (HFIR) [25,26,28–31] have investigated the microstructural evolution of W and W alloys. Their results indicate, for example, that the impact of transmutant Re and Os on the properties of materials after irradiation is at least as relevant as the displacement damage. Meanwhile, the current lack of experimental reactors and materials testing facilities that fully represent the conditions for making fusion a commercially feasible energy source has motivated multi-scale materials modeling efforts to investigate the irradiation and temperature effects expected in fusion power plants [32–50]. These approaches, frequently based on first-principles calculations, have demonstrated their ability to provide quantitative and qualitative predictions of the material behavior in such extreme environments.

Despite the recent experimental advances in Joyo, JMTR, and HFIR, and the numerous efforts in the literature to investigate the effects of alloying elements on various properties of W-based materials such as phase stability [51–55], elastic properties [51–54,56–58], ideal tensile strength [54,59], ductility [60], radiation defects [12,52,61], point defects [51,61–66], screw dislocation structures [67,68], grain boundaries [69], etc., to the best of our knowledge, there is still a lack of understanding on how the thermomechanical behavior of W-based PFMs change due to nuclear transmutation. In this work, we present a novel approach that integrates nuclear science and first-principles DFT electronic structure methods to better understand the neutron irradiation effects in PFMs. In particular, the goal of this study is to investigate how the bulk and mechanical properties of W-based SAs and HEAs evolve over time under neutron irradiation-induced transmutation.

Our paper is organized as follows. After this introduction, we provide in Section 2 an overview of the computational methods employed. The results are given in Section 3, which include: (i) the changes in the chemical composition during the course of irradiation due to transmutation; (ii) the calculation of the equilibrium lattice constant, elastic properties, density of states, generalized stacking fault energy, unstable stacking fault energy, gamma surface, and dislocation-based ductility parameter of five W-based candidate materials at the beginning of their operational life; and (iii) the effects of irradiation on these properties. We finalize in Section 4 with a brief discussion and the conclusions in Section 5.

## 2. Computational methods

The transmutation properties of W-based PFMs in a fusion-like environment were characterized by using the FISPACT-II inventory code developed and maintained by the United Kingdom Atomic Energy Authority over the last 30 years. FISPACT-II [19,20] solves coupled differential equations describing the rate of change of all possible nuclides and thus evolves a nuclide composition in time. For the present work, a $\phi(E)$ vector of neutron fluxes (as a function of energy $E$) was taken from neutron transport calculations performed for a recent conceptual design (see Fischer et al. [70], Gilbert et al. [71] for details) for EU-DEMO, a demonstration fusion power plant being researched in Europe [72,73]. Specifically, the energy-flux spectrum for the outer equatorial first wall of the torus-shaped tokamak has been used, which is predicted to be one of the highest flux regions of a fusion reactor (second only to the inner equator). The total flux $\phi$ for this spectrum was $2.1 \times 10^{14}$ n cm$^{-2}$ s$^{-1}$. FISPACT-II calculations evolved the initial composition of the five W-based materials shown in Table 1 in this neutron environment for 10 continuous full-power years.

Note for the present calculations, in contrast to those reported previously in Qian et al. [74], here self-shielding has been properly accounted for in the inventory simulations with FISPACT-II. This results in slightly reduced transmutation rates of certain elements, particularly W and Ta, which would otherwise have high burn-up rates due to over-predicted impact of giant neutron capture resonances, consequently leading to over-predicted production of transmutants such as Re – see Sublet et al. [19], Gilbert and Sublet [75], Gilbert et al. [76] for more details on the self-shielding phenomenon and the importance of including appropriate corrections in transmutation predictions of W and its periodic-table neighbors.

For their part, Density Functional Theory (DFT) calculations were performed by using the open-source software distribution QUANTUM ESPRESSO [78,79]. Following our recent work on first-principles calculations of transmuting W [74], we employed the local-density approximation (LDA) with the Perdew–Burke–Ernzerhof (PBE) parametrization [80] in the formulation of the exchange correlation functional. Furthermore, the virtual crystal approximation (VCA) [81] was used to simulate the variety of W-based alloys that result from transmutation. While this method presents technical limitations to study the role of the microstructure (not just the chemical composition), it is still a very efficient approach to investigate the broad range of chemical compositions proposed in this work. It has already been successfully used to investigate the evolution of mechanical properties with concentration [67,82]. For its part, optimized norm-conserving Vanderbilt pseudopotentials [83] compatible with VCA were used in our non-spin polarized calculations, as there is no experimental evidence about magnetic properties in the considered SAs and HEAs containing Cr. In particular, for the binary W-Cr system which is important in our study, there are no magnetic phases observed from its phase diagram [84]. We do not account for point defects in this work either.

The elastic properties were calculated using a conventional 2-atom bcc supercell, a shifted $22 \times 22 \times 22$ grid Monkhorst Pack $k$-mesh [85], and a planewave cutoff energy of 110 Ry ($\sim$ 1496.63 eV). For their part, the calculation of the gamma surfaces, generalized stacking fault energies (GSFE), and the dislocation-based ductility parameter were performed in a 14-atom bcc supercell, with an energy cutoff of 90 Ry ($\sim$ 1224.51 eV), and Brillouin zones sampled by a shifted $24 \times 24 \times 1$ grid. The reader is referred to our previous work [74] for more details on how we extract elastic and plastic properties from the energies calculated via DFT simulations.

## 3. Results

### 3.1. Nuclear transmutation

Figure 1 shows how the composition of the five W-based PFMs (initial compositions in Table 1) changed during the course of irradiation due to transmutation. The graph shows the concentrations on a logarithmic scale, both in atomic percent (at.%) and in atomic parts per million (appm), of the elements created during the course of the irradiation. Even after 10 years of irradiation, and despite W and Ta, in particular, being susceptible to high transmutation rates, all the W-based PFMs studied would still be predominantly composed of the elements in their initial chemical make-up.

**Table 1**
Chemical composition of the five W-based materials considered in this study at the beginning of their operational life.

| | Chemical composition (at%) | | | | | |
|---|---|---|---|---|---|---|
| | W | Cr | Ti | Y | Ta | V |
| Tungsten (W) | 100 | – | – | – | – | – |
| W smart alloy (SA1) [16] | 67.16 | 26.98 | 5.86 | – | – | – |
| W smart alloy (SA2) [17] | 67.93 | 31.11 | – | 0.958 | – | – |
| W high-entropy alloy (HEA1) [77] | 25 | 25 | 25 | – | 25 | – |
| W high-entropy alloy (HEA2) [77] | 25 | – | 25 | – | 25 | 25 |

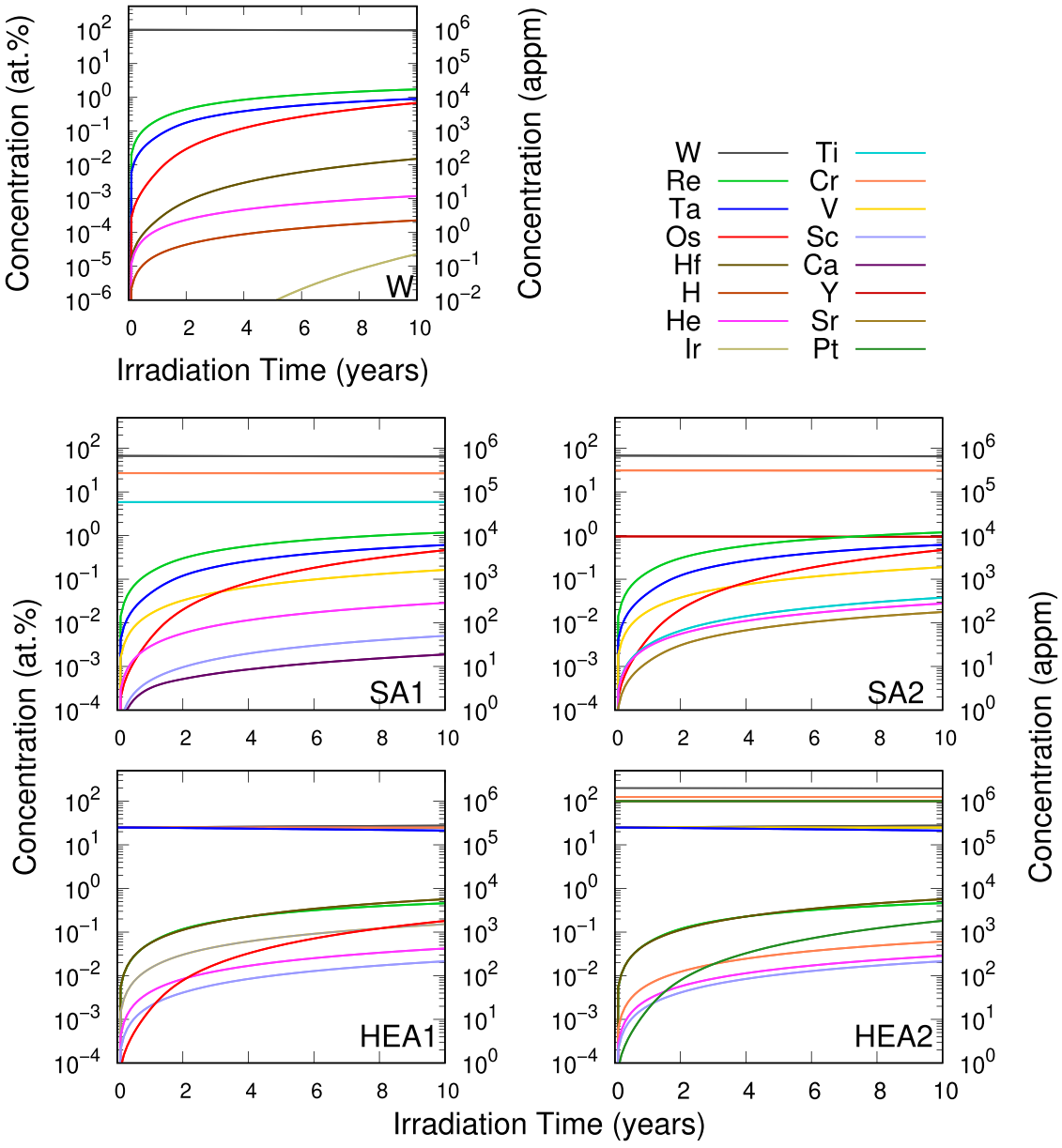


**Fig. 1.** Transmutation of W-based alloys during a 10-year irradiation in a fusion first wall.

To gain a deeper understanding of how the chemical composition changes during the course of irradiation we also plotted the concentration gradient $\Delta c = c(t) - c(0)$ in Fig. 2 for the top seven elements in each material, where $c(t)$ is the chemical composition after $t$ years of irradiation and $c(0)$ is the initial composition of the material. The elements included in the second plots of the transmutation results are the ones that will be considered in the formulation of the DFT pseudopotential in the following sections. The final compositions at 10 years of these alloys are listed in Table A.1. These results show how the profile of burn-up or growth of each element in the composition (both those originally present and those created by transmutation) varies for the different initial alloy compositions. For example, the rate of production of W decreases in pure W and W-SAs while it increases in the W-HEAs (due to its production from the burn-up of Ta in those alloys). The concentration of Re, a primary transmutant, increases in

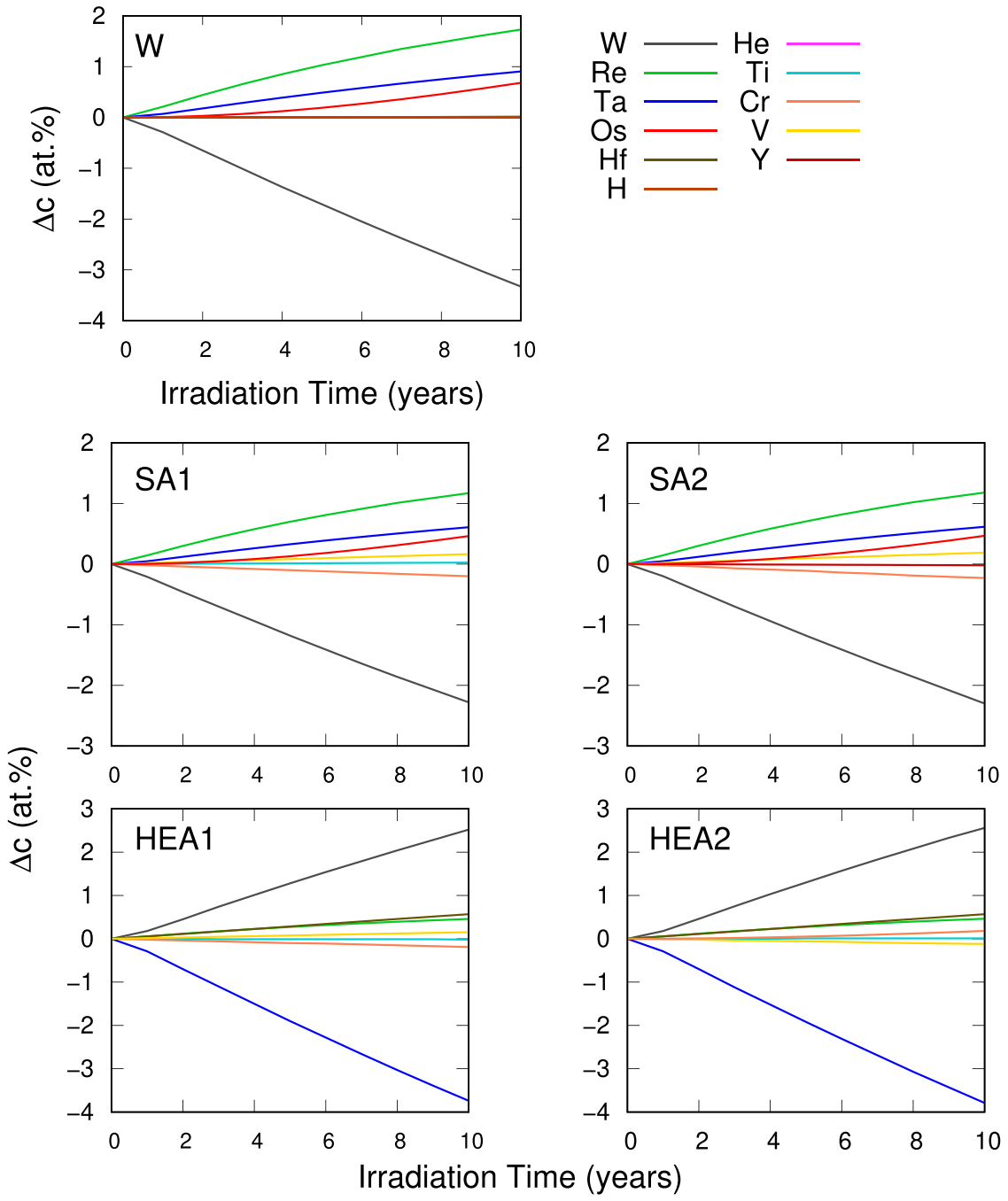


**Fig. 2.** Concentration gradient of W-based alloys during a 10-year fusion first wall irradiation. $\Delta c = c(t) - c(0)$, where $c(t)$ is the chemical composition after $t$ years of irradiation and $c(0)$ is the initial composition of the material.

all five materials (produced from W), while the concentration of Ta decreases (is burnt-up) in both W-HEAs (it is one of the initial alloying elements) and increases in pure W and the W-SAs.

As previously [74], we can obtain the time-averaged % errors in the transmutation predictions due to the evaluated uncertainties in the nuclear reaction data (from TENDL-2017 [86]). As standard, FISPACT-II computes errors in the concentrations of the dominant radionuclides in a material after irradiation, by summing in quadrature the uncertainty on each reaction in each production chain (or pathway) of the radionuclide. Typically, there may be several pathways of production for each nuclide; for example, after 10 years of irradiation, four reaction chains are found to be important for the production of $^{186}Re$ (half-life, $T_{1/2} = 3.7$ days) in pure W, involving various combinations of neutron capture (n,$\gamma$) and neutron multiplication (n,2n) reactions, as well as $\beta^-$ decay – FISPACT-II correctly combines the uncertainties across all chains and all reactions in each chain to calculate the overall uncertainty in $^{186}Re$.

For the present work, we have employed a modified version of FISPACT-II, where uncertainties are also evaluated for the production of stable nuclides of the main transmutant elements. The methodology is the same, whereby FISPACT-II uses a tree-search algorithm [19] to identify the contributing pathways for a given nuclide before propagating uncertainties along each chain, but here we enforce a requirement for even stable nuclides to receive this evaluation (this is not part of the usual methodology as FISPACT-

**Table 2**
Time-averaged % errors in elemental concentrations predicted by FISPACT-II for each component (original present elements and new transmutant products) in the alloys during the course of the 10-year power-plant first wall irradiation. Error estimates for transmutants are only given if their concentrations reach 1 appm during the 10 years (see main text for details).

| Material elements | W | SA1 | SA2 | HEA1 | HEA2 |
|---|---|---|---|---|---|
| W | 0.12‡ | 0.12‡ | 0.12‡ | 0.64‡ | 0.65‡ |
| Re | 9.15‡ | 9.07‡ | 9.08‡ | 8.64‡ | 8.57‡ |
| Ta | 36.20‡ | 36.22‡ | 36.22‡ | 0.22‡ | 0.22‡ |
| Os | 7.76‡ | 9.94‡ | 9.95‡ | 9.58 | 10.55‡ |
| Hf | 31.36‡ | 31.38 | 31.38 | 30.81‡ | 30.82‡ |
| He | 43.16‡ | 45.64 | 53.85 | 34.10 | 27.86 |
| H | 73.56‡ | 41.41 | 44.33 | 38.29 | 41.84 |
| Cr | – | 0.002‡ | 0.002‡ | 0.002‡ | 4.55 |
| Ti | – | 0.13‡ | 44.15 | 0.04‡ | 0.04‡ |
| V | – | 28.89‡ | 28.93‡ | 28.87‡ | 0.05‡ |
| Sc | – | 18.04 | – | 18.04 | 18.03 |
| Ca | – | 70.55 | – | 70.66 | 70.65 |
| Mn | – | 10.59 | 10.59 | 10.58 | – |
| Y | – | – | 0.01‡ | – | – |
| Sr | – | – | 35.62 | – | – |
| Zr | – | – | 6.72 | – | – |

‡ transmutation elements considered in pseudopotential generations of W-based alloys

II concentrates on evaluating activation uncertainties). To compute the final, total uncertainty of production for a complete element, we sum in quadrature the absolute uncertainties in concentration from the individual nuclides.

Table 2 shows the time-averaged (i.e. the average uncertainty in each element across the 10 different irradiation times) % uncertainties for each significant element (either original or transmutant) in the material. Note that the uncertainty quantification (UQ) approach used here, only calculates the *production* uncertainty on each nuclide (hence each element) – i.e. contributions to a nuclide's uncertainty only come from propagating uncertainties along reaction chains where that nuclide is a daughter. Uncertainties in the burn-up or *depletion* of nuclides as parents, which are particularly relevant for nuclides that are part of the initial composition of a material, are not included here (other than indirectly in the way those depletion uncertainties, represented by the initial reactions in each production chain, contribute to production uncertainties of daughters elsewhere). Future work will consider a methodology to combine production and depletion uncertainties for nuclides as, respectively, daughters and parents of nuclear reaction chains.

Notwithstanding the above caveat, it is clear from Table 2 that uncertainties are small for elements that were present in the initial compositions of the five materials, demonstrating that the growth rates for those elements, coming from the sum across all nuclides (stables and created unstables), are relatively small compared to the reservoir of original atoms of those elements.

On the other hand, for transmutant elements newly created by the irradiation exposure (compare Tables 1–A.1), where the production uncertainty is dominant, the results show that uncertainties in predictions can be reasonably high – as much as 70% in some cases. Such uncertainties are not uncommon in inventory predictions, particularly for minor (rare) components of a nuclide inventory, but it is vital that they are provided as part of any transmutation or activation analysis, both to appreciate the significance (or not) of the quantity to which they correspond, but also so that they could be used to define engineering safety factors in the design of fusion reactors. It has been observed, for example, that there is a potential 20–25% over-prediction compared to experimental measurements of the decay heat (measured in kW) in W after exposure to a fusion environment – in that case a low flux deuterium-tritium fusion neutron source (FNS) – where the primary reaction pathway responsible, $^{186}W(n,2n)^{185}W$, has a ~7% uncertainty in the FNS spectrum with TENDL-2017 (see Gilbert and Sublet [87], based on data from Gilbert and Sublet [88]); whilst an over-prediction is not ideal because the potential cost of unnecessary cooling engineering, such a prediction, with the data uncertainties, can be used to ensure sufficient cooling and thus safe reactor operation.

### 3.2. Material behavior at $t = 0$

In Table 3, we list the equilibrium lattice constant, single-crystal elastic constants, and polycrystalline elastic properties for five W-based PFMs at the beginning of their operational life, i.e. at time $t = 0$, with the chemical compositions shown in Table 1. While we could not find other works in the literature providing such a comprehensive study for the W-based alloys, Tables 2 and 3 in Qian et al. [74] show that the results obtained for pure W are consistent with their counterparts from previous experimental and theoretical works. These results also indicate the crucial role chemical composition plays in the elastic response of the material. For example, the elastic properties obtained for SA1 and SA2, whose chemical compositions still have W as the primary element (> 67 at.%), are closer to those from pure W, especially when compared with the four-component HEA1 and HEA2 equiatomic alloys.

While it was not possible to find experimental works in the literature comparing the properties listed in Table 3 for the exact W-based alloys studied in this work, the reader is referred to Tables A.5 and A.6 for a comparison with other experimental and theoretical works investigating HEAs and binary alloys with a similar composition. Firstly, the results of pure W [74] match well with both experimental [89] and theoretical [90,91] results. Secondly, our calculations for SAs indicate lower lattice constants and higher elastic properties when compared with pure W. This is in agreement with previous works in the literature. For example, Ma et al [91] also found, for a concentration of Cr of 6.25 at.% in W, that the lattice constant decreases, $C_{11}$ and $C_{44}$ increase, and $C_{12}$ decreases. Jiang et al [90] also did DFT calculations with 6.25 at.% of Cr, showing a smaller lattice constant, an increase of $C_{11}$, G, and E, and reduction of $C_{12}$, $C_{44}$, and B. They also found, however, that adding Cr up to 50 at.% would decrease all the elastic properties. The experimental results for W-Cr [92] and pure W [89] further confirm that a larger concentration of Cr will decrease all elastic properties of W. In our results, on the other hand, all elastic properties of SAs are higher than pure W. One reason for this may come from the fact that VCA didn't consider lattice distortion when introducing Cr. At lower concentrations of Cr, adding Cr will not generate large lattice distortion in pure W, where results of W-Cr below 6.25 at.% is increasing, which is similar to our results of $C_{11}$, G, and E. When adding more Cr, the impact of lattice distortion is not negligible.

In the case of high-entropy alloys (HEAs), our investigations into the elastic constants of WTiTaCr and WTiTaV alloys have yielded values within the same range as those found in other alloys, such as MoNbTaWV [93,116], MoNbTaTiV [94], NbTaTiWV [94] MoNbTaTiV [95] for parameters including $C_{11}$, $C_{44}$, B, G and E. Particularly, our calculations of E and the experimental results of $Mo_{\sim 0.8}(TaTiWZr)_{\sim 0.2}$ [96], TiZrHfNbV [97], MoTaTiW [98], TaTiWZr [98] follow a similar trend. Moreover, the effects of Ta and V in references [99] and [100] indicate that the addition of these elements to W would decrease the elastic constants, which agrees with our results of elastic constant for HEAs.

Figure 3 shows the generalized stacking fault energy (GSFE) curves on both $\langle 111 \rangle \{\bar{1}10\}$ and $\langle 111 \rangle \{11\bar{2}\}$ slip systems for the five W-based PFMs at the beginning of their operational life. The method used to calculate these properties is presented in detail in Ref. [74]. The figures reveal several interesting trends that are consistent with previous works in the field. Firstly, the unstable stack-

**Table 3**
Theoretical equilibrium lattice parameter, single-crystal elastic constants, and polycrystalline elastic properties for the five W-based PFMs at the beginning of their operational life, i.e., with the chemical compositions shown in Table 1: equilibrium lattice parameters $a_0$, bulk modulus $B$, elastic constants $C_{ij}$, tetragonal shear modulus $C'$, shear modulus $G$ and Young's modulus $E$.

| | $a_0$ (Å) | $C_{11}$ (GPa) | $C_{12}$ (GPa) | $C_{44}$ (GPa) | B (GPa) | $C'$ (GPa) | G (GPa) | E (GPa) |
|---|---|---|---|---|---|---|---|---|
| W | 3.1835 | 512.501 | 197.906 | 142.461 | 302.771 | 157.298 | 148.22 | 382.669 |
| SA1 | 3.100 | 554.167 | 212.469 | 166.285 | 326.369 | 170.849 | 151.011 | 392.496 |
| SA2 | 3.093 | 571.430 | 218.195 | 181.037 | 335.940 | 176.618 | 161.594 | 417.793 |
| HEA1 | 3.144 | 351.731 | 195.262 | 107.702 | 247.419 | 78.235 | 86.934 | 233.460 |
| HEA2 | 3.199 | 285.202 | 178.625 | 99.756 | 214.151 | 53.289 | 72.234 | 194.802 |

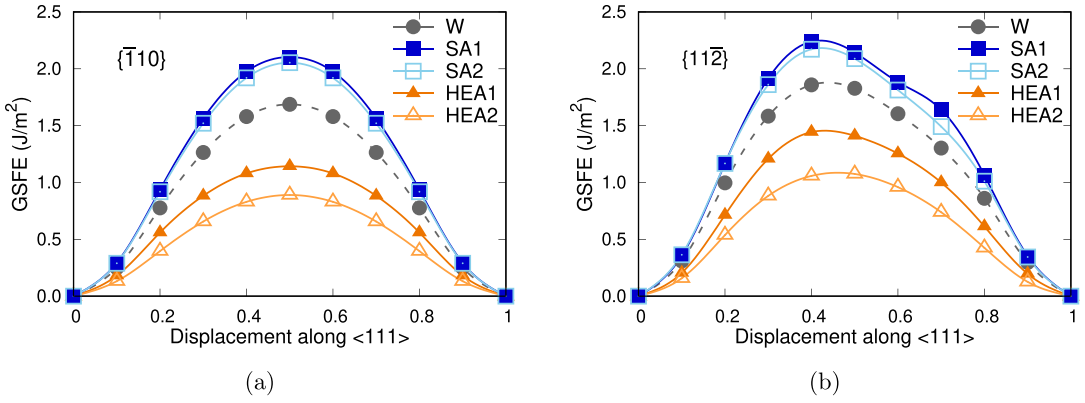


**Fig. 3.** The general stacking fault energy for the initial composition of the five candidate PFMs along (a) {111}{$\bar{1}$10} and (b) {111}{11$\bar{2}$}.

**Table 4**
Theoretical surface energy $\gamma_s$, unstable stacking fault energy $\gamma_{us}$, and dislocation-based ductility parameter $D$ for the five W-based PFMs at the beginning of their operational life, i.e., with the chemical compositions shown in Table 1. The calculations have been performed in both {111}{$\bar{1}$10} and {111}{11$\bar{2}$} slip systems.

| | ⟨111⟩{$\bar{1}$10} | | | ⟨111⟩{11$\bar{2}$} | | |
|---|---|---|---|---|---|---|
| | $\gamma_s$ (J/m$^2$) | $\gamma_{us}$(J/m$^2$) | D | $\gamma_s$(J/m$^2$) | $\gamma_{us}$(J/m$^2$) | D |
| W | 3.308 | 1.687 | 1.961 | 3.762 | 1.875 | 2.006 |
| SA1 | 3.869 | 2.103 | 1.839 | 4.474 | 2.243 | 1.994 |
| SA2 | 3.874 | 2.054 | 1.887 | 4.447 | 2.178 | 2.042 |
| HEA1 | 2.959 | 1.143 | 2.590 | 3.583 | 1.489 | 2.406 |
| HEA2 | 2.888 | 0.890 | 3.246 | 3.450 | 1.085 | 3.179 |

ing fault energy $\gamma_{us}$, defined as the maximum value of the GSFE curve, is always in the middle of the energy path from one equilibrium position to another on a {$\bar{1}$10} plane while there is certain asymmetry towards the first equilibrium position on a {11$\bar{2}$} plane [60,101–105]. Secondly, $\gamma_{us}$ is higher for the ⟨111⟩{11$\bar{2}$} slip system [52,60,104–106]. Thirdly, taking pure W as a reference, we notice that the GSFE curve is lower for HEA1 and HEA2, and higher for SA1 and SA2. The specific values of $\gamma_{us}$ are shown in Table 4, which also includes the surface energy $\gamma_s$ and the dislocation-based ductility parameter $D = \frac{\gamma_s}{\gamma_{us}}$ formulated by Rice [107]. The effects of the chemical composition on the calculated $\gamma_s$ are similar to those observed for $\gamma_{us}$, i.e., if we take pure W as the reference system, HEA1 and HEA2 have an inferior $\gamma_s$, while SA1 and SA2 present a superior value. This implies, as it is shown in Table 4, that the dislocation-based ductility parameter $D$ is higher in W-HEAs and lower in W-SAs.

The impact of the alloying elements on the electronic structure of the five W-based PFMs at the beginning of their operational life can be investigated via the total density of states (TDOS), which is shown in Fig. 4. One can recognize, for W and the other alloys, the shape of the $d$ band with a marked pseudo-gap, as expected for BCC transition metals. To compare the different alloys,

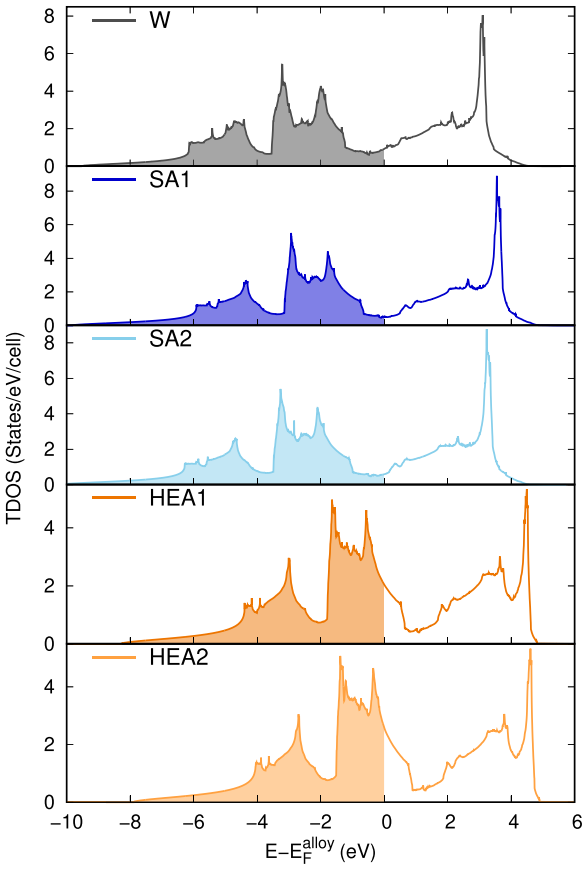


**Fig. 4.** Total DOS of the candidate W-based materials at the beginning of their operational life. $E_F^{alloy}$ is the Fermi energy of each material (see Table 5), and is taken as the reference energy.

**Table 5**
Fermi energy $E_F^{alloy}$, number of valence electrons, and TDOS values at Fermi energies for each of the five W-based PFMs at time $t = 0$.

| | $E_F^{alloy}$ (eV) | No. valence e$^-$ | $TDOS_F$ |
|---|---|---|---|
| W | 21.942 | 14 | 0.855 |
| SA1 | 21.771 | 13.883 | 0.545 |
| SA2 | 22.287 | 13.971 | 0.590 |
| HEA1 | 18.902 | 13.250 | 2.055 |
| HEA2 | 17.858 | 13 | 2.604 |

the Fermi energy of each material $E_F^{alloy}$ is taken as the reference energy. $E_F^{alloy}$ values are listed in Table 5, together with the number of valence electrons for each of the candidate PFMs. These results reveal the different nature of the two families of W-based alloys studied here: W-SAs show slight variations of the valence charge and the Fermi level compared to pure W, with a Fermi level located in the pseudogap, while the decrease of valence charge for W-HEAs is more significant, lowering the Fermi energy. This results in a shift of the Fermi level of HEAs to the left, outside the pseudo gap, which is evident in Fig. 4.

The reader is referred to Appendix A (Table A.4, A.2 and A.3, and Figure A.1) for more details about the material behavior of the principal alloying elements of the W-based PFMs shown in Table 1: Cr, Ta, Ti, and V. These include their equilibrium lattice parameter, single-crystal elastic constants, surface energy, unstable stacking fault energy, dislocation-based ductility parameter, Fermi energy, and TDOS, among others.

### 3.3. Effects of irradiation on the behavior of tungsten-based PFMs

Given the extreme environments that PFMs will be exposed to in a fusion device, it is critical to understand both their behavior at $t = 0$ (cf. Section 3.2) and how their response evolves due to the changes in the chemical composition that occur through nuclear transmutation (cf. Section 3.1).

Our results for the changes in equilibrium lattice constant, single-crystal elastic constants, and polycrystalline elastic properties due to transmutation on the five W-based PFMs after 10 years of exposure are listed in Table 6.

Notice that the changes in these properties over time are less pronounced than the existing differences between the families of W-based alloys before any irradiation occurs. As such, we do not plot the absolute trends here. Instead, we choose to provide the initial and final values in Table 3 and Table 6, and represent the time evolution of the aforementioned properties in terms of the relative difference $\delta_X$, defined as:

$$\delta_X = \frac{X_t - X_0}{X_0} \tag{1}$$

where $X_0$ is the value of the property of interest $X$ at the beginning of the operational life of the material (t = 0 years) and $X_t$ is the value of that same property after $t$ years of exposure to the fusion conditions described in Section 2.

Following this notation, Figs. 5 and 6 show the time dependence of the equilibrium lattice constant, single-crystal elastic constants, and polycrystalline elastic properties as the chemical compositions of the W-based materials change due to irradiation. The observed linear behavior has been confirmed in previous experimental [108] and computational [54,67] measurements of W-Re alloys, as well as in our recent calculations on transmuting W [74]. In advance of discussing these results and their implications in detail in the following section, we note the following features from the figures:

(i) the relative difference $\delta$ after ten years of exposure is less than 7% for all the properties investigated;
(ii) the lattice constant is the only measurement decreasing for all five W-based PFMs as irradiation time (and therefore the relative concentration of transmutants) increases. $C_{12}$ and $C'$ show some materials with a flat or slightly negative slope. All other properties are seen to monotonically increase with irradiation time for all five W-based PFMs;
(iii) the magnitude of the slope is steeper for W-HEAs than for W-SAs. In particular, HEA2 presents the most prominent changes with irradiation for the majority properties and SA2 the smallest.

To illustrate the effects of nuclear transmutation on the electronic structure of the candidate PFMs, we plot in Fig. 7 the total DOS of pure W and transmuted W after ten years of continuous exposure to EU-DEMO first wall conditions. These results indicate that the Fermi energy slightly increases after ten years, but the shape of the $d$ band remains essentially unchanged after irradiation.

Given the small differences between the total DOS for pure W and transmuted W after 10 years of irradiation shown in Fig. 7, we plot in Fig. 8 the relative difference of the integrated TDOS, named $\delta_{iDOS}$[1], to show the effect of transmutation for the five W-based PFMs after 10 years of irradiation.

The magnitude of maximum peak is always less than 1.5% indicating that the differences between the integrated TDOS over the entire energy range are very small. Despite these slight variations, we can still appreciate how the regions with a positive slope indicate an energy range where the integrated TDOS of transmuted PFMs is higher than its counterpart at $t = 0$, or vice versa.

Next, we calculate the evolution of the number of valence electrons during the first ten years of irradiation. The results are shown in Fig. 9 for all five W-based PFMs. Given that the observed changes in the absolute number of valence electrons are less pronounced than the inherent differences between the families of W-based alloys before any irradiation occurs, we decided to provide the initial values in Table 5 and represent the time evolution of the valence electrons in terms of the relative difference $\delta$ used before for the elastic properties (cf Eq. (1)). Based on these results, all materials increased their number of valence electrons over time, and W-HEAs show a steeper slope than W-SAs. Still, these behaviors should be taken in context, as the relative differences are always less than 0.3%.

In Fig. 10, we provide the evolution of $\gamma_{us}$ and $\gamma_s$ for both $\langle 111\rangle\{\bar{1}10\}$ and $\langle 111\rangle\{11\bar{2}\}$ slip systems during the first ten years of irradiation under EU-DEMO first wall conditions. We choose to represent the irradiation effects on these properties in terms of the relative % difference $\delta$ for the same reasons discussed above when presenting the evolution of the elastic properties and the number of valence electrons. Several trends can be identified from these figures. Firstly, the changes on the $\gamma_{us}$ are twice as pronounced as the changes on $\gamma_s$. That applies to all the materials and both slip systems. Secondly, the $\delta$ values of both properties are higher on the $\{11\bar{2}\}\langle 111\rangle$ slip system for all the materials. Thirdly, a different evolution is observed depending on the chemical composition of the W-based alloys. Both $\gamma_{us}$ and $\gamma_s$ monotonically increase on both slip systems for W-HEAs while they decrease or remain flat (depending on the property) for W-SAs. Furthermore, the magnitude of the slope is always steeper for W-HEAs than for W-SAs. For its part, W presents a more similar behavior to W-SAs, decreasing its $\gamma_{us}$ and slightly decreasing its $\gamma_s$ due to transmutation.

Once the irradiation effects on both $\gamma_s$ and $\gamma_{us}$ are calculated, the relative difference of the dislocation-based ductility parame-

[1] The relative difference $\delta_{iDOS}$ is defined as $\delta_{iDOS} = \frac{iDOS_t - iDOS_0}{iDOS_0}$, where $iDOS_t$ and $iDOS_0$ are the integrated DOS of materials after 10 years irradiation and for the initial composition, respectively.

**Table 6**
Theoretical equilibrium lattice parameter, single-crystal elastic constants, and polycrystalline elastic properties for the five W-based PFMs at $t = 10$: equilibrium lattice parameters $a_0$, bulk modulus $B$, elastic constants $C_{ij}$, tetragonal shear modulus $C'$, shear modulus (G) and Young's modulus (E).

| | $a_0$ (Å) | $C_{11}$ (GPa) | $C_{12}$ (GPa) | $C_{44}$ (GPa) | B (GPa) | $C'$ (GPa) | G (GPa) | E (GPa) |
|---|---|---|---|---|---|---|---|---|
| W | 3.181 | 514.148 | 200.873 | 144.994 | 305.298 | 156.638 | 149.544 | 385.900 |
| SA1 | 3.098 | 557.410 | 212.331 | 168.265 | 327.357 | 172.540 | 152.708 | 396.475 |
| SA2 | 3.092 | 572.320 | 218.743 | 181.961 | 336.602 | 176.789 | 162.195 | 419.246 |
| HEA1 | 3.139 | 358.815 | 197.354 | 108.453 | 251.174 | 80.731 | 88.286 | 237.082 |
| HEA2 | 3.192 | 293.897 | 180.507 | 101.412 | 218.304 | 56.695 | 74.639 | 201.007 |

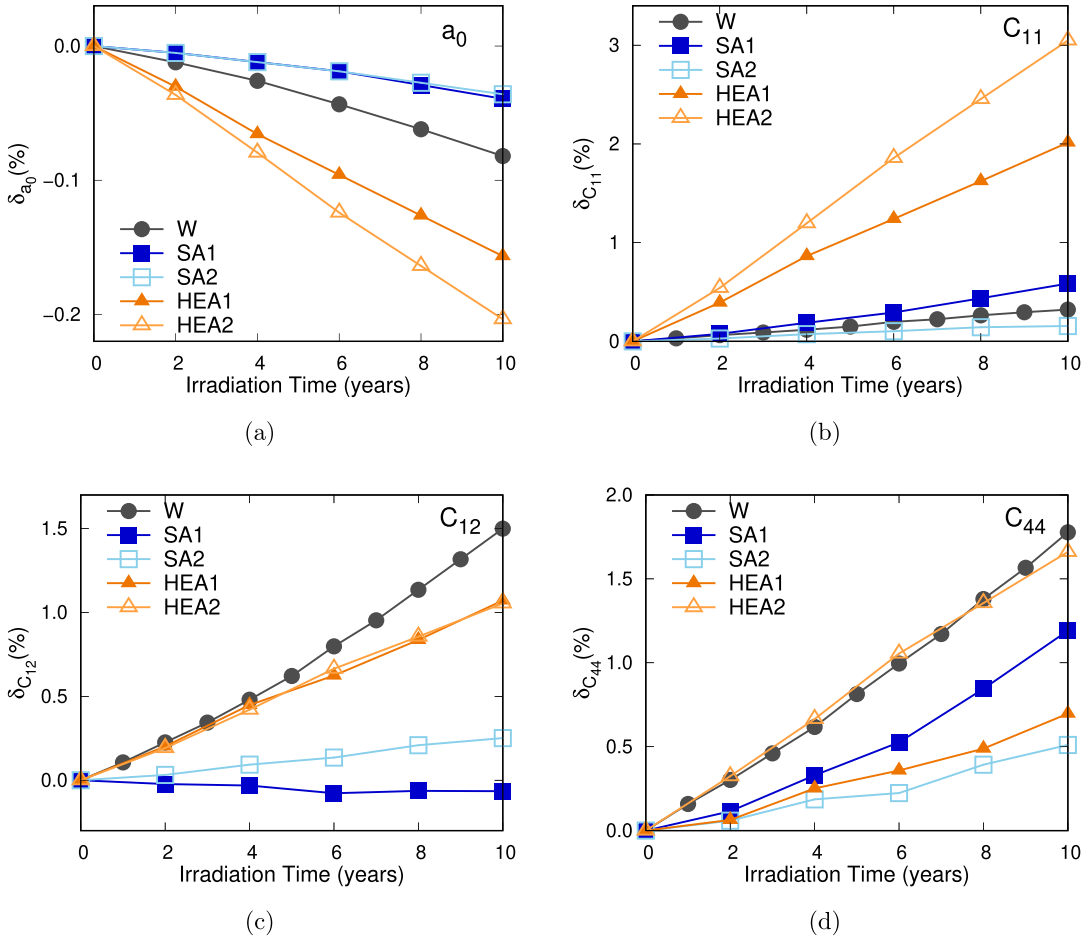


**Fig. 5.** Evolution of (a) the lattice constant $a_0$ and the elastic properties (b) $C_{11}$, (c) $C_{12}$, (d) $C_{44}$ during the first ten years of irradiation under EU-DEMO first wall conditions.

ter $D = \frac{\gamma_s}{\gamma_{us}}$ [107] is obtained. We present results for the two slip systems of interest in Fig. 11. All the materials exhibit a linear behavior with irradiation time: W is the material with the steepest increase of ductility, followed by SA2; the variations on SA1 are negligible, while both W-HEAs show a decrease of ductility, with HEA2 being the material experiencing the most significant drop. It is also worth noting that the increase on ductility for W and the W-SAs is more pronounced on the $\{\bar{1}10\}\langle 111\rangle$ slip system.

## 4. Discussion

### 4.1. Material behavior at the beginning of the operational life

Section 3.2 presented the behavior of the W-based PFMs before exposing them to a plasma-exposed environment expected in EU-DEMO. The results included calculations of the lattice parameter, elastic properties, general stacking fault energies, unstable stacking fault energies, gamma surfaces, dislocation-based ductility parameter, total DOS, Fermi energy, and number of valence electrons.

First, the comparison of the overall behavior of the two families of W-based PFMs reveal that W-SAs present more similarities to pure W than W-HEAs. These observations, shown for example when comparing the total DOS in Fig. 4, are consistent with the chemical composition of the candidate materials and the fundamental nature of the VCA approach: the W-HEAs studied here are four-element equiatomic HEAs and the W-SAs contain a higher relative concentration of W.

Next, if we take pure W as the reference material, understanding why specific properties increase for W-HEAs and decrease for W-SAs, and vice versa, requires a more profound discussion supported by the study of the underlying effects of the individual alloying elements and their relative composition. For this purpose, we also investigated, in Appendix A (Table A.2, A.3 and A.4, Figure A.1), the material behavior of the principal alloying ele-

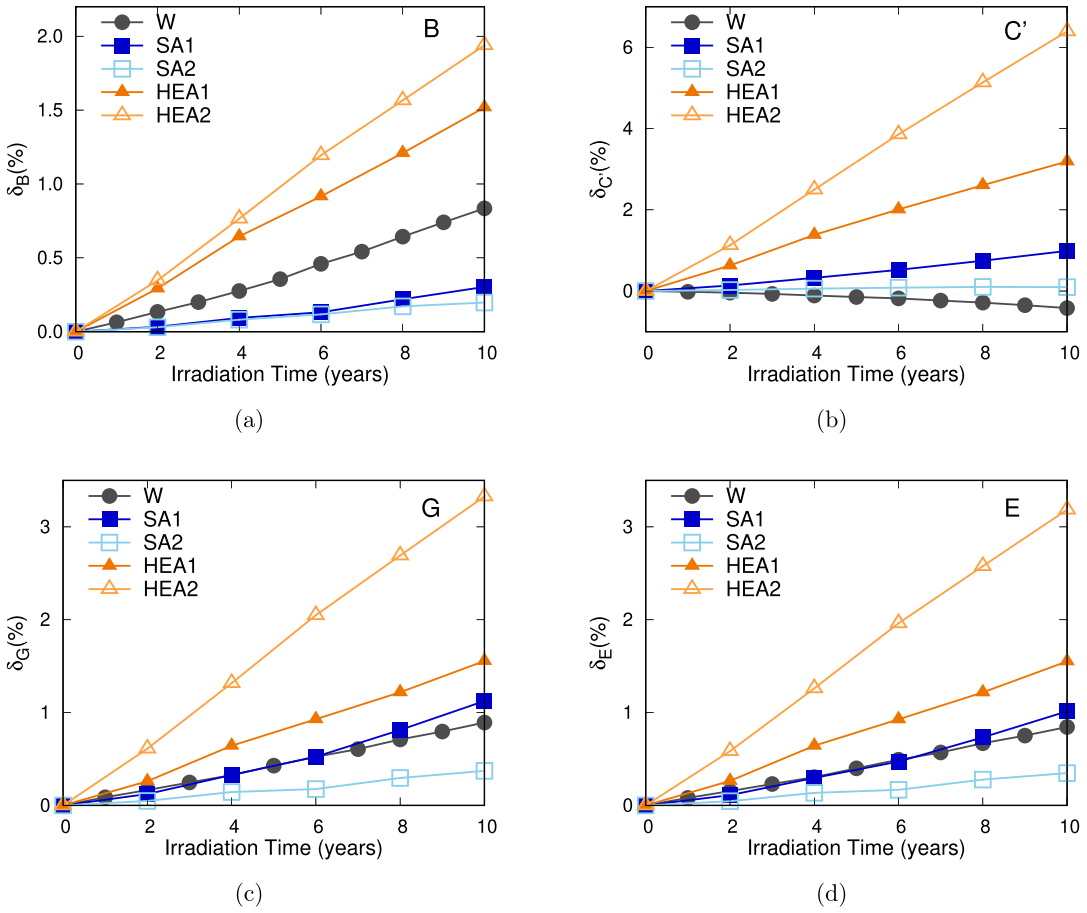


**Fig. 6.** Evolution of (a) the bulk modulus $B$, (b) the tetragonal shear elastic constant $C'$, (c) the shear modulus $G$, and (d) the Young's modulus $E$ during the first ten years of irradiation under EU-DEMO first wall conditions.

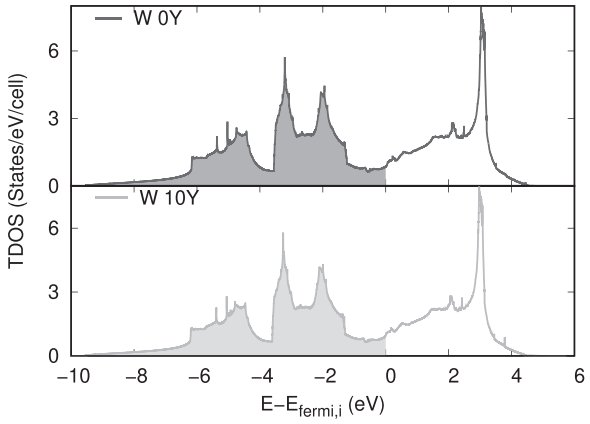


**Fig. 7.** Comparison of the total DOS for pure W and transmuting W after 10 years or irradiation. $E_{ref}$ is the Fermi energy of pure W. Top: total DOS of pure W; Bottom: total DOS of transmuting W after 10 years of irradiation.

ments, i.e.: Cr, Ta, Ti, and V. The results for W and the alloys, shown in Tables 3, 4 and Fig. 3 reveal that the lattice constant is higher in W-HEAs, while all the other elastic properties and GSFE are higher in W-SAs. One contributing factor, suggested by the data in Table A.2, to these differences could be the presence of Ti in the W-HEAs: Ti, in a bcc phase, has negative elastic constants since its stable phase at low temperature is hcp.

Furthermore, the comparison between the two W-HEAs indicates that HEA2 is softer than HEA1. We find this consistent with the presence of V in HEA2 and Cr in HEA1 (cf. Table 1). The softer behavior of V with respect to Cr (cf. Table A.2), the expected hardening effect when reducing the lattice constant (cf. Table A.2), and the relative changes in hardening when comparing different columns in the periodic table (V is Group V while Cr is group VI), are all indicators that softening in the HEA2 in comparison to HEA1 would be expected.

In terms of GSFE, $\gamma_{us}$, and the dislocation-based ductility parameter $D$, the presence of the different alloying elements (cf. Table 1) and their individual properties (as shown in Table A.3) also play a critical role in explaining the behavior of the different W-based candidate materials. For example, the presence of Ta in HEAs and its lower $\gamma_{us}$ with respect to pure W (cf. Table A.3) reduces $\gamma_{us}$ of HEAs when compared to pure W and SAs. Similar to the behavior observed with the elastic properties, the presence of V in HEA2 reduces its $\gamma_{us}$ when compared to HEA1, which, instead, contains Cr.

The total electronic density of states (TDOS) shown in Fig. 4 allows us to better understand the physical origin of stabilization of the alloys. Specifically, the Fermi energy, number of electrons, and the TDOS at the Fermi energy of each material are strongly correlated with the physical properties, as listed in Table 5. From Table 5 and Fig. 4, it is clear that the Fermi energies of W and SAs, which are located at DOS values of 0.855, 0.545, and 0.590 for W, SA1, and SA2, respectively, are located in valleys of the TDOS, thus

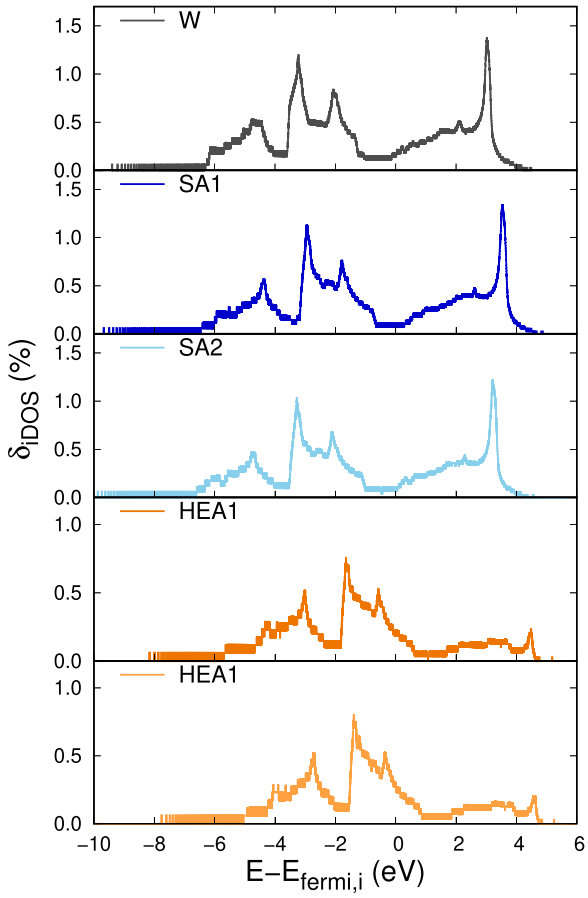


**Fig. 8.** Relative difference $\delta$ of the integrated TDOS for the five W-based PFMs after 10 years or irradiation.

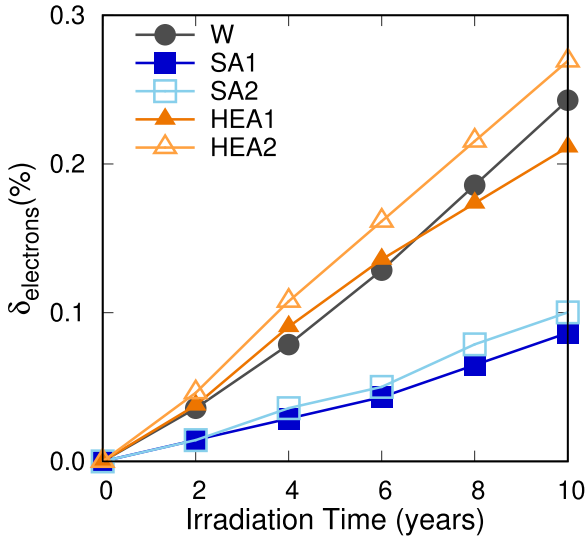


**Fig. 9.** % change in the number of valence electrons for the five W-based PFMs during the ten years of irradiation under EU-DEMO first wall conditions.

implying that the structures of these should be stable. Conversely, the Fermi energies of HEAs at 2.055 and 2.604 for HEA1 and HEA2, respectively, are located in regions of steep gradient in the TDOS distributions, indicating that the HEA structures will destabilize. In general, a lower TDOS value at the Fermi energy corresponds to a raising of the surface energy and the unstable stacking energy for both HEAs and SAs, excluding the surface energies of {111} {$\bar{1}$10} between SA1 and SA2.

### 4.2. Effects of irradiation on the behavior of tungsten-based PFMs

The inventory simulation results in Figs. 1 and 2 show that the composition of W and W-based alloys will evolve significantly under irradiation, which motivated the exploration of how these changes could impact on properties. Table 2 goes further with the FISPACT-II simulations by including an assessment of the uncertainties associated with the predicted concentrations of each transmutant, which originate from the errors provided alongside the nuclear data library evaluations for individual reaction cross sections. For the TENDL library used in the calculations, uncertainty quantification is performed using Bayesian Monte Carlo (BMC), which combines uncertainties reported in the experimental data with the uncertainties in the nuclear models that are fitted to produce the cross section evaluations, see [109,110] for details.

The estimates in Table 2 show that the uncertainties can be significant and should be factored in to any discussion of the significance of transmutation predictions in neutron-irradiated materials.

The variation in elastic properties of pure W and W-based alloys as a function of irradiation time were plotted in Fig. 5. The number of valence electrons per atom of alloys is determined by its composition by using VCA method. From Fig. 9, one can see that the number of valence electrons for the five W-base PFMs will increase with irradiation time.

The total electronic density of states (TDOS) shown in Fig. 4 showed that the Fermi energies of the HEAs before irradiation are located in high gradient regions of the TDOS. The irradiation is predicted to add valence electrons to the materials, leading to a shift of the Fermi energy to higher energy levels, closer to a valley. In this case, materials with the initially lower Fermi energy will become more stable, in good agreement with the increasing elastic properties of HEAs as well as the greater increase for HEA2 than HEA1 (more valence electrons). Meanwhile, the relatively slight change of valence electrons of SAs produces a small change of elastic properties compared to HEAs (apart from the variation in $C_{44}$ of SA1).

The reduction of lattice constant and the enlargement of bulk modulus are consistent with experimental measurements and *d*-band filling predictions [108] of valence electron increases. Furthermore, a larger reduction of lattice constant seems to lead to a larger increase in the bulk modulus (cf. Fig. 5(a) and (b)).

The relative change in surface energies and unstable stacking fault energies as function of irradiation time of W, HEAs and SAs are shown in Fig. 10. The Rice criterion [107] was used to estimate the ductility of materials using the ratio of $\gamma_s$ and $\gamma_{us}$, shown in Fig. 11. Materials with a larger ratio will prefer to allow slip of atomic layers under external stresses, while a smaller ratio implies a material that would rather crack to generate a new surface [111–113]. In Fig. 10, both $\gamma_s$ and $\gamma_{us}$ of HEAs show an increase as function of irradiation. This behavior can be explained based on the variation of the number of electrons up to 10 years. According to Figs. 9 and 4, HEA2 experiences a relatively higher increase in valence electrons than HEA1, becoming more stable with irradiation time, and thus having higher changes in relative $\gamma_{us}$ values. Similarly, from Figs. 9 and 4, the electrons increase with irradiation time for SAs and W. However, the Fermi energy is initially located in a valley of TDOS for these materials and further increasing the number of electrons (i.e. with irradiation time) will tend to push the Fermi energy towards regions of high gradient in the TDOS, most prominently for SA2 and W, while the change is negligible for SA1. In this case, materials would become more unstable, and this is consistent with the decrease in $\gamma_{us}$ of W and SA2, while there is almost no change for SA1.

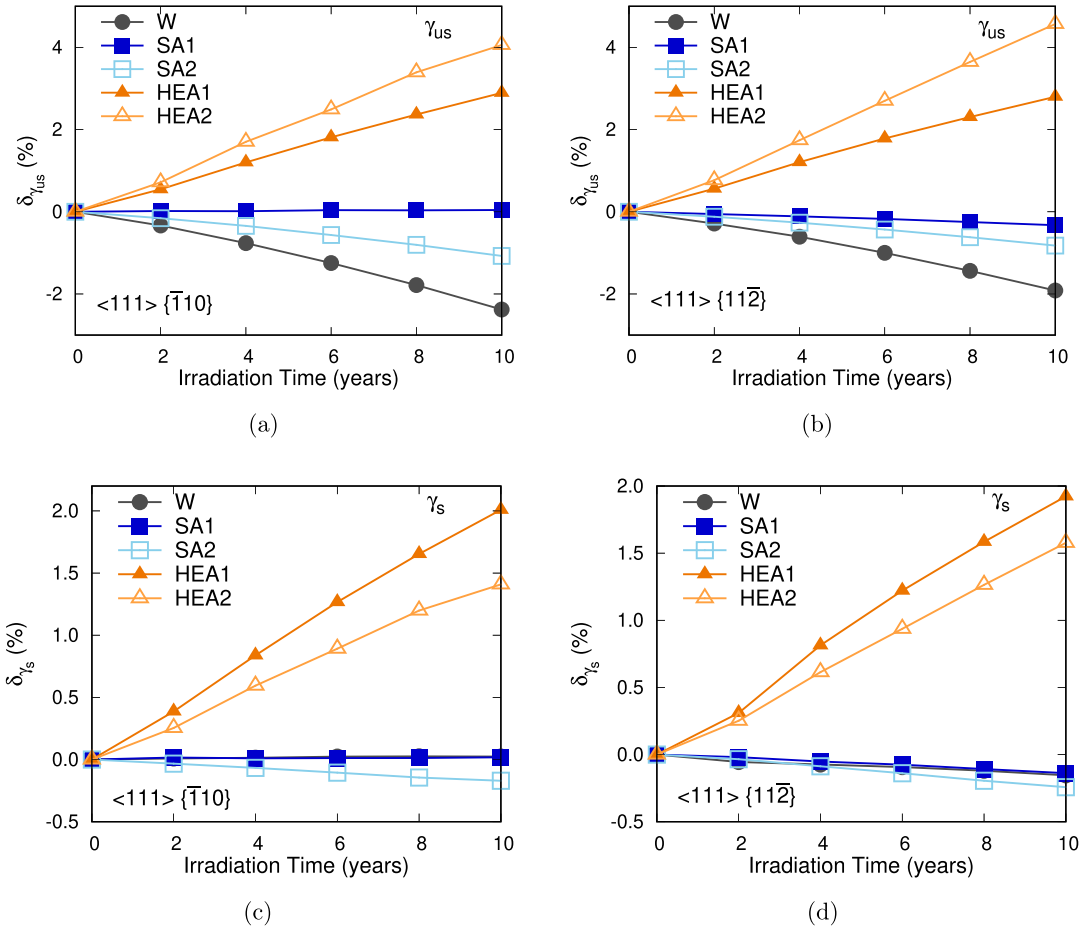


**Fig. 10.** % evolution of the unstable stacking fault energy $\gamma_{us}$ for the (a) $\{\bar{1}10\}\langle 111\rangle$, and (b) $\{11\bar{2}\}\langle 111\rangle$ slip systems, and the corresponding surface energy $\gamma_s$ for (c) $\{\bar{1}10\}\langle 111\rangle$, and (d) $\{11\bar{2}\}\langle 111\rangle$, during ten years of irradiation under EU-DEMO first wall conditions.

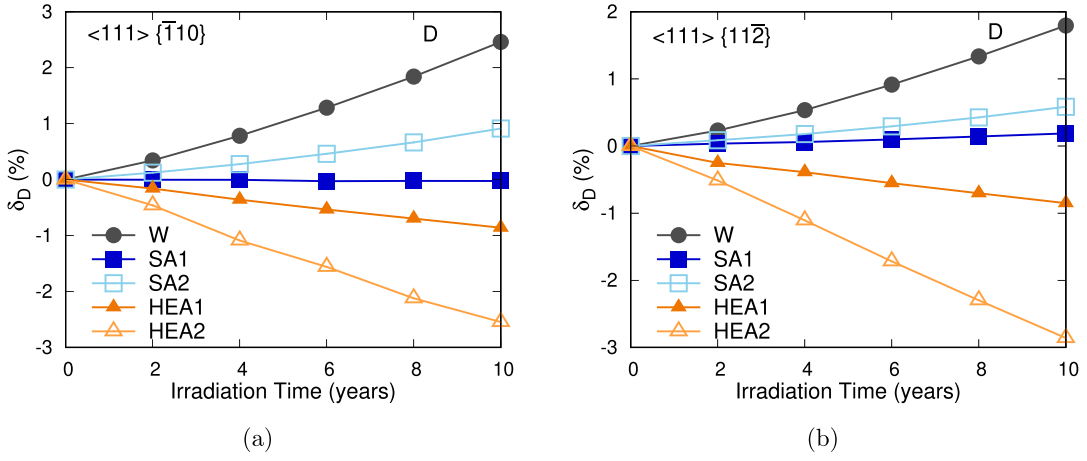


**Fig. 11.** Evolution of the dislocation-based ductility parameter $D$ for the five W-based materials along the (a) $\langle 111\rangle\{\bar{1}10\}$ and (b) $\langle 111\rangle\{11\bar{2}\}$ slip systems during the first ten years of continuous exposure to EU-DEMO first wall conditions.

As we mentioned in Section 3, the changes to $\gamma_{us}$ are twice as pronounced as the changes to $\gamma_s$, implying that $\gamma_{us}$ is the major factor to govern the dislocation-based ductility parameter $D$ of SAs and HEAs for both slip systems. The results of the ductility parameter are shown in Fig. 11. This figure shows that HEAs are likely to become more brittle with irradiation time, while irradiation will tend to enhance the ductility of W and SA2, for both slip systems considered. SA1 did not show any significant variation as a function of irradiation time. From Fig. 2, it can be deduced that the increasing ductility of W and SA2 comes from the reduction of W and the increase of Re in the materials. The increase in brittleness of the HEAs is due to the loss of Ta and the corresponding generation of W under transmutation. The relative differences in the rates of change in concentration of these HEAs during irradiation could

explain the different rates of change in properties observed. HEA1 shows a Cr reduction of 0.19 atomic % and the generation of 0.15% V, while HEA2 loses 0.12% V and creates 0.18% Os (cf. Tables 1 and A.1). Therefore, HEA2 experiences a higher decrease of $\delta_D$ compared to HEA1 because it shows a transmutation drift from Group V (Vanadium) to Group VIII (Os), while HEA1 shows only a group V to Group VI drift (V to Cr).

## 5. Conclusions

We studied how mechanical properties of five W-based PFMs (including pure W) evolve under irradiation using the FISPACT-II inventory code coupled with DFT simulations with the VCA approximation.

First, we found that uncertainties in transmutation prediction from nuclear simulations can be significant, particularly for the newly created transmutants elements in these W alloys. This observation highlights the importance of correct uncertainty propagation in such simulations. Even though the irradiation-induced composition changes are not predicted to have a significant impact on material properties in the present work, it will not always be the case. For example, changes in thermal conductivity as a function of transmutation are striking in W [114], and DFT approaches (different from VCA) that investigate the heterogenous distribution of alloying elements instead of defining virtual atoms with a homogeneous distribution might predict a more significant impact on the material properties compared to those found here. In such cases, it will be vital to include the uncertainties in predictions of material performance – using the method exemplified here. So far, these calculations only include uncertainties in nuclear reactions propagated along the reaction chains from starting isotope parents to their daughters that contribute to the evolving elemental composition. In the future, the analysis should be extended to include data-induced uncertainties in neutron transport simulations (already mature, see e.g. Kos et al. [115]) as well as the uncertainties in designs of fusion reactors, such as geometry variation and material (composition) selection. Not only will a more complete error propagation give greater confidence to the predictions, but it will also identify the key (dominant) sources of uncertainty that should be the focus of future (uncertainty) reduction efforts.

Our results also suggest that the differences in the properties of the four W-based candidate alloys at the beginning of their operation life are more significant than the changes induced by irradiation. However, this observation might be an artefact of the VCA approach, which assumes a homogeneous distribution of the alloying elements within the definition of the virtual atoms. The formulation is a limiting factor of the current method, which prevents a proper investigation, particularly, of the role of the microstructure (not necessarily the chemical composition) on the mechanical behavior of these materials. A deep understanding of microstructural damage in alloys under neutron irradiation needs further theoretical and experimental investigations. Previous works in the literature have compared the VCA approach with SQS for other HEAs, such as NbMoTaW and NbMoTaWV [116]. They reported a relative error of the elastic properties calculated here that ranges from [0–10.2] % for NbMoTaW and [0.06–24.5]% for NbMoTaWV. Our current and future efforts are directed towards studying more complete first-principles DFT electronic structure methods to effectively predict the phase stability and the mechanical properties of irradiated plasma-facing materials.

## Declaration of Competing Interest

The authors declare that they have no known competing financial interests or personal relationships that could have appeared to influence the work reported in this paper.

## CRediT authorship contribution statement

**Yichen Qian:** Investigation, Methodology, Software, Visualization, Formal analysis, Writing – original draft, Writing – review & editing. **Mark R. Gilbert:** Conceptualization, Investigation, Methodology, Software, Supervision, Writing – original draft, Writing – review & editing. **Lucile Dezerald:** Supervision, Visualization, Writing – review & editing. **Duc Nguyen-Manh:** Supervision, Writing – review & editing. **David Cereceda:** Conceptualization, Funding acquisition, Methodology, Visualization, Supervision, Investigation, Resources, Writing – original draft, Writing – review & editing.

## Data availability

Data will be made available on request.

## Acknowledgments

This work used the Extreme Science and Engineering Discovery Environment (XSEDE), which is supported by National Science Foundation grant number ACI-1548562. Specifically, YQ and DC acknowledge support from XSEDE allocation MAT200015. YQ and DC also acknowledge computer time allocations at Villanova's Augie and Alipi clusters. DC acknowledges support from the U.S. Department of Energy, Office of Science, Fusion Energy Sciences Program Early Career Research Program under Award Number DE-SC0023072. MRG and DNM acknowledge funding from the EPSRC Energy Programme [Grant number EP/W006839/1]. DNM work has also been carried out within the framework of the EUROfusion Consortium, funded by the European Union via the Euratom Research and Training Programme (Grant agreement no. 101,052,200 EUROfusion). Views and opinions expressed are however those of the author(s) only and do not necessarily reflect those of the European Union or the European Commission. Neither the European Union nor the European Commission can be held responsible for them. LD acknowledges support from LabEx DAMAS (program investissements dAvenir ANR-11-LABX-008-01). This work received funding from Villanova University's Falvey Memorial Library Scholarship Open Access Reserve (SOAR) Fund.

## Appendix A. Material behavior of the principal alloying elements

**Table A.1**
Compositions of W and W-alloys after the 10-year fusion power-plant first wall irradiation (atomic % concentration units) as predicted by FISPACT-II.

| Material elements | W | SA1 | SA2 | HEA1 | HEA2 |
|---|---|---|---|---|---|
| W | 9.666E + 01 | 6.481E + 01 | 6.555E + 01 | 2.748E + 01 | 2.753E + 01 |
| Re | 1.727 | 1.159 | 1.182 | 4.574E−01 | 4.614E−01 |
| Ta | 9.061E−01 | 6.076E−01 | 6.145E−01 | 2.122E + 01 | 2.119E + 01 |
| Os | 6.822E−01 | 4.614E−01 | 4.665E−01 | 1.799E−01 | 1.814E−01 |
| Hf | 1.517E−02 | 1.017E−02 | 1.029E−02 | 5.671E−01 | 5.667E−01 |
| He | 1.198E−03 | 2.863E−02 | 2.766E−02 | 4.207E−02 | 2.857E−02 |
| H | 5.718E−03 | 1.197E−01 | 1.252E−01 | 1.550E−01 | 1.232E−01 |
| Cr | – | 2.675E + 01 | 3.084E + 01 | 2.477E + 01 | 6.095E−02 |
| Ti | – | 5.877 | 3.773E−02 | 2.495E + 01 | 2.498E + 01 |
| V | – | 1.635E−01 | 1.885E−01 | 1.515E−01 | 2.485E + 01 |
| Sc | – | 5.025E−03 | 2.941E−07 | 2.412E−02 | 2.144E−02 |
| Ca | – | 1.881E−03 | 7.655E−06 | 7.995E−03 | 7.993E−03 |
| Mn | – | 1.578E−04 | 1.818E−04 | 1.463E−04 | 2.71E−012 |
| Y | – | – | 9.375E−01 | – | – |
| Sr | – | – | 1.767E−02 | – | – |
| Zr | – | – | 1.103E−03 | – | – |

**Table A.2**
Theoretical equilibrium lattice parameter, single-crystal elastic constants, and polycrystalline elastic properties for the principal initial alloying elements of the W-based PFMs (see Table 1) equilibrium lattice parameters $a_0$, bulk modulus $B$, elastic constants $C_{ij}$, tetragonal shear modulus $C'$, shear modulus (G) and Young's modulus (E).

| | $a_0$ (Å) | $C_{11}$ (GPa) | $C_{12}$ (GPa) | $C_{44}$ (GPa) | B (GPa) | $C'$ (GPa) | G (GPa) | E (GPa) |
|---|---|---|---|---|---|---|---|---|
| W | 3.1835 | 512.501 | 197.906 | 142.461 | 302.771 | 157.298 | 148.22 | 382.669 |
| Cr | 2.850 | 491.795 | 143.543 | 101.429 | 259.627 | 174.126 | 95.416 | 255.008 |
| Ta | 3.320 | 262.579 | 159.921 | 72.436 | 194.140 | 51.329 | 47.812 | 132.554 |
| Ti | 3.262 | 87.367 | 113.411 | 39.409 | 104.730 | -13.022 | -0.300 | -0.900 |
| V | 3.000 | 264.370 | 138.842 | 23.738 | 180.685 | 62.764 | 26.548 | 75.925 |

**Table A.3**
Theoretical surface energy $\gamma_s$, unstable stacking fault energy $\gamma_{us}$, and dislocation-based ductility parameter $D$ for elements used in the PFMs considered in this work (see Table 1). The calculations have been performed in both $\{111\}\{\bar{1}10\}$ and $\{111\}\{11\bar{2}\}$ slip systems.

| | System | This work | | | References | | |
|---|---|---|---|---|---|---|---|
| | | $\gamma_s$ (J/m$^2$) | $\gamma_{us}$(J/m$^2$) | D | $\gamma_s$(J/m$^2$) | $\gamma_{us}$(J/m$^2$) | D |
| $\langle 111\rangle\{\bar{1}10\}$ | W | 3.308 | 1.684 | 1.961 | 3.181 [60] | 1.633 [60] | |
| | Cr | 3.308 | 1.530 | 2.163 | 3.505 [117] | 1.570 [118] | |
| | Ta | 2.502 | 0.724 | 3.387 | 2.685 [119] | 0.831 † [120] | |
| | V | 2.788 | 0.751 | 3.713 | 2.428 [121] | 0.616 [121] | 3.93 [121] |
| $\langle 111\rangle\{11\bar{2}\}$ | W | 3.762 | 1.875 | 2.006 | 3.367 [60] | 1.830 [60] | |
| | Cr | 3.772 | 1.599 | 2.359 | 3.892 [117] | 1.634 [118] | |
| | Ta | 3.004 | 0.871 | 3.370 | 2.884 [119] | 0.977 † [120] | |
| | V | 3.214 | 0.895 | 3.591 | 2.703 [121] | 0.719 [121] | 3.76 [121] |

† Spectral neighbor analysis potential

**Table A.4**
Fermi energy $E_F$ and number of valence electrons for the principal alloying elements of the W-based PFMs.

| | $E_{F,i}$ (eV) | No. valence e$^-$ |
|---|---|---|
| W | 21.942 | 14 |
| Cr | 19.652 | 14 |
| Ti | 13.370 | 12 |
| Ta | 18.106 | 13 |
| V | 16.628 | 13 |

**Table A.5**
Comparison of the theoretical equilibrium lattice parameter, single-crystal elastic constants, and polycrystalline elastic properties between the W-based SAs studied in this work (at the beginning of their operational life) and other experimental and theoretical results found in the literature for similar chemical compositions. Values for pure W are provided as a reference.

| | DFT Method | $a_0$ (Å) | $C_{11}$ (GPa) | $C_{12}$ (GPa) | $C_{44}$ (GPa) | B (GPa) | G (GPa) | E (GPa) |
|---|---|---|---|---|---|---|---|---|
| | | | | Present work[†] | | | | |
| W | VCA | 3.184 | 512.5 | 197.91 | 142.46 | 302.77 | 148.22 | 382.67 |
| $W_{0.67}Cr_{0.27}Ti_{0.06}$(SA1) | VCA | 3.100 | 554.17 | 212.47 | 166.26 | 326.37 | 151.01 | 392.5 |
| $W_{0.68}Cr_{0.31}Y_{0.01}$ (SA2) | VCA | 3.091 | 571.43 | 218.2 | 181.04 | 335.94 | 161.59 | 417.79 |
| | | | | Experimental results | | | | |
| W [89] | | 3.165 | 532.55 | 204.95 | 163.13 | 314.15 | 163.4 | 417.76 |
| $W_{0.9}Cr_{0.1}$ [92] | | | | | | 262.7 | 132.7 | 340.7 |
| | | | | Computational results | | | | |
| W [90] | | 3.176 | 523.4 | 211.4 | 140.5 | 315.4 | 146.7 | 380.1 |
| $W_{15}Cr_1$ [90] | SC[‡] | 3.160 | 531.0 | 200.1 | 138.7 | 310.4 | 149.4 | 386.2 |
| $W_{12}Cr_4$ [90] | SC[‡] | 3.106 | 511.9 | 189.4 | 120.9 | 299.11 | 137.0 | 356.3 |
| $W_{0.9375}Cr_{0.0625}$ [91] | SC[‡] | 3.157 | 593.34 | 183.92 | 146.61 | | | |

[1] Computational software used in calculations is indicated through the following symbols: [†]Quantum Espresso; [‡] VASP.
[2] The acronyms used for the DFT methods listed in the table are: Supercell (SP), Virtual Crystal Approximation (VCA).

**Table A.6**
Comparison of the theoretical equilibrium lattice parameter, single-crystal elastic constants, and polycrystalline elastic properties between the W-based HEAs studied in this work (at the beginning of their operational life) and other experimental and theoretical results found in the literature for similar chemical compositions. Values for pure W are provided as a reference.

| | DFT Method | $a_0$ (Å) | $C_{11}$ (GPa) | $C_{12}$ (GPa) | $C_{44}$ (GPa) | B (GPa) | G (GPa) | E (GPa) |
|---|---|---|---|---|---|---|---|---|
| | | | | Present work[†] | | | | |
| W | VCA | 3.184 | 512.5 | 197.91 | 142.46 | 302.77 | 148.22 | 382.67 |
| WCrTiTa (HEA1) | VCA | 3.144 | 351.73 | 195.26 | 107.7 | 247.42 | 86.93 | 233.46 |
| WTiTaV (HEA2) | VCA | 3.199 | 285.2 | 178.63 | 99.76 | 214.15 | 72.23 | 194.8 |
| | | | | Experimental results | | | | |
| W [89] | | 3.165 | 532.55 | 204.95 | 163.13 | 314.15 | 163.4 | 417.76 |
| $Mo_{\sim 0.8}(TaTiWZr)_{\sim 0.2}$ [96] | | | | | | | | 255.65 |
| TiZrHfNbV [97] | | | | | | | | 128 |
| TaTiWZr [98] | | | | | | | | 168.65 |
| MoTaTiW [98] | | | | | | | | 199.23 |
| | | | | Computational results | | | | |
| W [90] | SC[‡] | 3.176 | 523.4 | 211.4 | 140.5 | 315.4 | 146.7 | 380.1 |
| MoNbTaTiV [95] | SQS[‡] | | 262.03 | 141.45 | 43.22 | 181.2 | 50.71 | 139.15 |
| MoNbTaTiV [94] | SQS[*] | | 303.5 | 135.9 | 22 | 190 | 47.08 | 130.5 |
| NbMoTaW [116] | SQS[**] | 3.193 | 392 | 158 | 79 | 236 | 92 | 245 |
| NbMoTaW [116] | VCA[**] | 3.195 | 425 | 158 | 86 | 247 | 102 | 270 |
| NbMoTaWV [116] | SQS[**] | 3.165 | 379 | 143 | 65 | 222 | 82 | 200 |
| NbMoTaWV [116] | VCA[**] | 3.167 | 421 | 144 | 72 | 236 | 94 | 249 |
| NbMoTaWV [93] | SQS[*] | | 392.73 | 160.0 | 57.6 | 234.0 | 81.1 | 218.0 |
| NbTaTiWV [94] | SQS[*] | | 321.5 | 142.4 | 107.1 | 198.6 | 100.1 | 257.3 |
| $W_{0.30}(TaTiVCr)_{0.70}$ [122] | SQS[‡] | | | | | 215.28 | 60.08 | 164.89 |

[1] Computational software used in calculations is indicated through the following symbols: [†]Quantum Espresso; [‡] VASP; [*]CP2K; [**]Castep.
[2] The acronyms used for the DFT methods listed in the table are: Supercell (SP), Virtual Crystal Approximation (VCA), Special Quasirandom Structures (SQS).

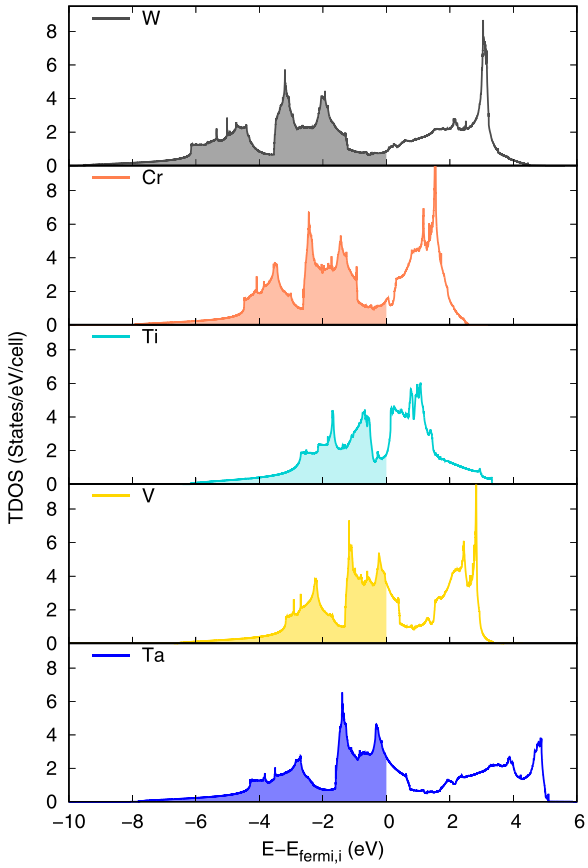


**Fig. A.1.** Total DOS of the alloying elements of SAs and HEAs. $E_{F,i}$ is the Fermi energy of each material, and it is taken as the reference energy.

## References


[1] S.J. Zinkle, N.M. Ghoniem, Prospects for accelerated development of high performance structural materials, J. Nucl. Mater. 417 (1) (2011) 2–8.

[2] M.-H. Tsai, J.-W. Yeh, High-entropy alloys: a critical review, Mater. Res. Lett. 2 (3) (2014) 107–123.

[3] Z. Li, K.G. Pradeep, Y. Deng, D. Raabe, C.C. Tasan, Metastable high-entropy dual-phase alloys overcome the strength–ductility trade-off, Nature 534 (7606) (2016) 227–230.

[4] E.P. George, D. Raabe, R.O. Ritchie, High-entropy alloys, Nat. Rev. Mater. 4 (8) (2019) 515–534.

[5] B.S. Murty, J.-W. Yeh, S. Ranganathan, P. Bhattacharjee, High-Entropy Alloys, Elsevier, 2019.

[6] J.-W. Yeh, S.-K. Chen, S.-J. Lin, J.-Y. Gan, T.-S. Chin, T.-T. Shun, C.-H. Tsau, S.-Y. Chang, Nanostructured high-entropy alloys with multiple principal elements: novel alloy design concepts and outcomes, Adv. Eng. Mater. 6 (5) (2004) 299–303.

[7] Z. Leong, J.S. Wrbel, S.L. Dudarev, R. Goodall, I. Todd, D. Nguyen-Manh, The effect of electronic structure on the phases present in high entropy alloys, Sci. Rep. 7 (2017) 39803.

[8] O.A. Waseem, H.J. Ryu, Powder metallurgy processing of a WxTaTiVCr high-entropy alloy and its derivative alloys for fusion material applications, Sci. Rep. 7 (1) (2017) 1–14.

[9] Y. Zou, H. Ma, R. Spolenak, Ultrastrong ductile and stable high-entropy alloys at small scales, Nat. Commun. 6 (1) (2015) 1–8.

[10] O.N. Senkov, D.B. Miracle, K.J. Chaput, J.-P. Couzinie, Development and exploration of refractory high entropy alloysa review, J. Mater. Res. 33 (19) (2018) 3092–3128.

[11] O. El-Atwani, A. Alvarado, K. Unal, S. Fensin, J. Hinks, G. Greaves, J. Baldwin, S. Maloy, E. Martinez, Helium implantation damage resistance in nanocrystalline W-Ta-V-Cr high entropy alloys, Mater. Today Energy 19 (2021) 100599.

[12] O. El-Atwani, N. Li, M. Li, A. Devaraj, J. Baldwin, M.M. Schneider, D. Sobieraj, J.S. Wróbel, D. Nguyen-Manh, S.A. Maloy, et al., Outstanding radiation resistance of tungsten-based high-entropy alloys, Sci. Adv. 5 (3) (2019) eaav2002.

[13] O.N. Senkov, G. Wilks, J. Scott, D.B. Miracle, Mechanical properties of Nb25Mo25Ta25W25 and V20Nb20Mo20Ta20W20 refractory high entropy alloys, Intermetallics 19 (5) (2011) 698–706.

[14] A. Litnovsky, F. Klein, X. Tan, J. Ertmer, J. Coenen, C. Linsmeier, J. Gonzalez-Julian, M. Bram, I. Povstugar, T. Morgan, Y.M. Gasparyan, A. Suchkov, D. Bachurina, D. Nguyen-Manh, M.G. Gilbert, D. Sobieraj, J.S. Wrbel, E. Tejado, J. Matejicek, K. Zoz, H. Benz, P. Bittner, A. Reuban, Advanced self-passivating alloys for an application under extreme conditions, Metals 11 (2021) 1255.

[15] D. Sobieraj, J. Wrbel, M.R. Gilbert, A. Litnovsky, F. Klein, K.J. Kurzydowski, D. Nguyen-Manh, Composition stability and Cr-rich phase formation in W-Cr-Y and W-Cr-Ti smart alloys, Metals 11 (2021) 743.

[16] A. Litnovsky, T. Wegener, F. Klein, C. Linsmeier, M. Rasinski, A. Kreter, B. Unterberg, M. Vogel, S. Kraus, U. Breuer, et al., Smart alloys for a future fusion power plant: first studies under stationary plasma load and in accidental conditions, Nucl. Mater. Energy 12 (2017) 1363–1367.

[17] F. Klein, M.R. Gilbert, A. Litnovsky, J. Gonzalez-Julian, S. Weckauf, T. Wegener, J. Schmitz, C. Linsmeier, M. Bram, J.W. Coenen, Tungsten–chromium–yttrium alloys as first wall armor material: yttrium concentration, oxygen content and transmutation elements, Fusion Eng. Des. 158 (2020) 111667.

[18] F. Koch, H. Bolt, Self passivating W-based alloys as plasma facing material for nuclear fusion, Phys. Scr. 2007 (T128) (2007) 100.

[19] J.-Ch. Sublet, J.W. Eastwood, J.G. Morgan, M.R. Gilbert, M. Fleming, W. Arter, FISPACT-II: an advanced simulation system for activation, transmutation and material modelling, Nucl. Data Sheets 139 (2017) 77–137.

[20] M. Fleming, T. Stainer, M.R. Gilbert, The FISPACT-II User Manual, Technical report, UKAEA, 2018. Available from http://fispact.ukaea.uk

[21] T. Tanno, A. Hasegawa, J. He, M. Fujiwara, M. Satou, S. Nogami, K. Abe, T. Shishido, Effects of transmutation elements on the microstructural evolution and electrical resistivity of neutron-irradiated tungsten, J. Nucl. Mater. 386 (2009) 218–221.

[22] T. Tanno, M. Fukuda, S. Nogami, A. Hasegawa, Microstructure development in neutron irradiated tungsten alloys, Mater. Trans. 52 (2011) 1105231402.

[23] M. Fukuda, T. Tanno, S. Nogami, A. Hasegawa, Effects of re content and fabrication process on microstructural changes and hardening in neutron irradiated tungsten, Mater. Trans. 53 (12) (2012) 2145–2150.

[24] M. Fukuda, A. Hasegawa, T. Tanno, S. Nogami, H. Kurishita, Property change of advanced tungsten alloys due to neutron irradiation, J. Nucl. Mater. 442 (1–3) (2013) S273–S276.

[25] A. Hasegawa, T. Tanno, S. Nogami, M. Satou, Property change mechanism in tungsten under neutron irradiation in various reactors, J. Nucl. Mater. 417 (1–3) (2011) 491–494.

[26] A. Hasegawa, M. Fukuda, K. Yabuuchi, S. Nogami, Neutron irradiation effects on the microstructural development of tungsten and tungsten alloys, J. Nucl. Mater. 471 (2016) 175–183.

[27] M. Fujitsuka, B. Tsuchiya, I. Mutoh, T. Tanabe, T. Shikama, Effect of neutron irradiation on thermal diffusivity of tungsten–rhenium alloys, J. Nucl. Mater. 283 (2000) 1148–1151.

[28] L.M. Garrison, Y. Katoh, J.W. Geringer, M. Akiyoshi, X. Chen, M. Fukuda, A. Hasegawa, T. Hinoki, X. Hu, T. Koyanagi, et al., Phenix US-Japan collaboration investigation of thermal and mechanical properties of thermal neutron–shielded irradiated tungsten, Fusion Sci. Technol. 75 (6) (2019) 499–509.

[29] T. Hwang, A. Hasegawa, K. Tomura, N. Ebisawa, T. Toyama, Y. Nagai, M. Fukuda, T. Miyazawa, T. Tanaka, S. Nogami, Effect of neutron irradiation on rhenium cluster formation in tungsten and tungsten-rhenium alloys, J. Nucl. Mater. 507 (2018) 78–86.

[30] Y. Katoh, L. Snead, L. Garrison, X. Hu, T. Koyanagi, C. Parish, P. Edmondson, M. Fukuda, T. Hwang, T. Tanaka, et al., Response of unalloyed tungsten to mixed spectrum neutrons, J. Nucl. Mater. 520 (2019) 193–207.

[31] P.D. Edmondson, B. Gault, M.R. Gilbert, An atom probe tomography and inventory calculation examination of second phase precipitates in neutron irradiated single crystal tungsten, Nucl. Fusion 60 (12) (2020) 126013.

[32] D. Nguyen-Manh, A. Horsfield, S. Dudarev, Self-interstitial atom defects in bcc transition metals: group-specific trends, Phys. Rev. B 73 (2) (2006) 020101.

[33] P.M. Derlet, D. Nguyen-Manh, S. Dudarev, Multiscale modeling of crowdion and vacancy defects in body-centered-cubic transition metals, Phys. Rev. B 76 (5) (2007) 054107.

[34] D. Nguyen-Manh, V. Vitek, A. Horsfield, Environmental dependence of bonding: a challenge for modelling of intermetallics and fusion materials, Prog. Mater. Sci. 52 (2–3) (2007) 255–298.

[35] D. Nguyen-Manh, M.Y. Lavrentiev, M. Muzyk, S. Dudarev, First-principles models for phase stability and radiation defects in structural materials for future fusion power-plant applications, J. Mater. Sci. 47 (21) (2012) 7385–7398.

[36] D. Cereceda, J.M. Perlado, J. Marian, Techniques to accelerate convergence of stress-controlled molecular dynamics simulations of dislocation motion, Comput. Mater. Sci 62 (2012) 272–275.

[37] S. Dudarev, Density functional theory models for radiation damage, Annu. Rev. Mater. Res. 43 (2013) 35–61.

[38] D. Cereceda, Multiscale Modeling of the Plastic Behaviour in Single Crystal Tungsten: From Atomistic to Crystal Plasticity Simulations, Univerisdad Politécnica de Madrid, 2015 Ph.D. thesis.

[39] F. Hofmann, D. Nguyen-Manh, M. Gilbert, C. Beck, J. Eliason, A. Maznev, W. Liu, D. Armstrong, K. Nelson, S. Dudarev, Lattice swelling and modulus change in a helium-implanted tungsten alloy: X-ray micro-diffraction, surface acoustic wave measurements, and multiscale modelling, Acta Mater. 89 (2015) 352–363.

[40] D. Nguyen-Manh, S. Dudarev, Trapping of he clusters by inert-gas impurities in tungsten: first-principles predictions and experimental validation, Nucl. Instrum. Methods Phys. Res., Sect. B 352 (2015) 86–91.

[41] D. Cereceda, M. Diehl, F. Roters, D. Raabe, J.M. Perlado, J. Marian, Unraveling the temperature dependence of the yield strength in single-crystal tungsten using atomistically-informed crystal plasticity calculations, Int. J. Plast. 78 (2016) 242–265.

[42] S.G. De Vicente, J.-L. Boutard, S. Zinkle, H. Tanigawa, Materials testing facilities and programmes for fission and ion implantation damage, Nucl. Fusion 57 (9) (2017) 092011.
[43] R. Abernethy, Predicting the performance of tungsten in a fusion environment: a literature review, Mater. Sci. Technol. 33 (4) (2017) 388–399.
[44] J. Marian, C.S. Becquart, C. Domain, S.L. Dudarev, M.R. Gilbert, R.J. Kurtz, D.R. Mason, K. Nordlund, A.E. Sand, L.L. Snead, et al., Recent advances in modeling and simulation of the exposure and response of tungsten to fusion energy conditions, Nucl. Fusion 57 (9) (2017) 092008.
[45] D.R. Mason, D. Nguyen-Manh, C.S. Becquart, An empirical potential for simulating vacancy clusters in tungsten, J. Phys. 29 (50) (2017) 505501.
[46] S.L. Dudarev, D.R. Mason, E. Tarleton, P.-W. Ma, A.E. Sand, A multi-scale model for stresses, strains and swelling of reactor components under irradiation, Nucl. Fusion 58 (12) (2018) 126002.
[47] D.R. Mason, D. Nguyen-Manh, M.-C. Marinica, R. Alexander, A.E. Sand, S.L. Dudarev, Relaxation volumes of microscopic and mesoscopic irradiation-induced defects in tungsten, J. Appl. Phys. 126 (7) (2019) 075112.
[48] K. Nordlund, Historical review of computer simulation of radiation effects in materials, J. Nucl. Mater. 520 (2019) 273–295.
[49] P.M. Derlet, S.L. Dudarev, Microscopic structure of a heavily irradiated material, Phys. Rev. Mater. 4 (2020) 023605.
[50] M.R. Gilbert, K. Arakawa, Z. Bergstrom, M.J. Caturla, S.L. Dudarev, F. Gao, A. Goryaeva, S. Hu, X. Hu, R.J. Kurtz, et al., Perspectives on multiscale modelling and experiments to accelerate materials development for fusion, J. Nucl. Mater. 554 (2021) 153113.
[51] M. Muzyk, D. Nguyen-Manh, K.J. Kurzydłowski, N.L. Baluc, S.L. Dudarev, Phase stability, point defects, and elastic properties of W-V and W-Ta alloys, Phys. Rev. B 84 (2011) 104115.
[52] M. Muzyk, D. Nguyen-Manh, J. Wróbel, K. Kurzydłowski, N. Baluc, S. Dudarev, First-principles model for phase stability, radiation defects and elastic properties of W–Ta and W–V alloys, J. Nucl. Mater. 442 (1–3) (2013) S680–S683.
[53] N. Wei, T. Jia, X. Zhang, T. Liu, Z. Zeng, X. Yang, First-principles study of the phase stability and the mechanical properties of W-Ta and W-re alloys, AIP Adv. 4 (5) (2014) 057103.
[54] C. Yang, L. Qi, Ab initio calculations of ideal strength and lattice instability in W-Ta and W-Re alloys, Phys. Rev. B 97 (1) (2018) 014107.
[55] C.-H. Huang, L. Gharaee, Y. Zhao, P. Erhart, J. Marian, Mechanism of nucleation and incipient growth of Re clusters in irradiated W-Re alloys from kinetic monte carlo simulations, Phys. Rev. B 96 (9) (2017) 094108.
[56] D. Jiang, C. Ouyang, S. Liu, Mechanical properties of W–Ti alloys from first-principles calculations, Fusion Eng. Des. 106 (2016) 34–39.
[57] X. Li, S. Schönecker, R. Li, X. Li, Y. Wang, J. Zhao, B. Johansson, L. Vitos, Ab initio calculations of mechanical properties of bcc W–Re–Os random alloys: effects of transmutation of W, J. Phys. 28 (29) (2016) 295501.
[58] Y.-J. Hu, S.-L. Shang, Y. Wang, K.A. Darling, B.G. Butler, L.J. Kecskes, Z.-K. Liu, Effects of alloying elements and temperature on the elastic properties of W-based alloys by first-principles calculations, J. Alloys Compd. 671 (2016) 267–275.
[59] S. Giusepponi, M. Celino, The ideal tensile strength of tungsten and tungsten alloys by first-principles calculations, J. Nucl. Mater. 435 (1–3) (2013) 52–55.
[60] J. Qian, C. Wu, J. Fan, H. Gong, Effect of alloying elements on stacking fault energy and ductility of tungsten, J. Alloys Compd. 737 (2018) 372–376.
[61] D. Nguyen-Manh, J.S. Wróbel, M. Klimenkov, M.J. Lloyd, L. Messina, S.L. Dudarev, First-principles model for voids decorated by transmutation solutes: short-range order effects and application to neutron irradiated tungsten, Phys. Rev. Mater. 5 (2021) 065401.
[62] T. Suzudo, M. Yamaguchi, A. Hasegawa, Stability and mobility of rhenium and osmium in tungsten: first principles study, Modell. Simul. Mater. Sci. Eng. 22 (7) (2014) 075006.
[63] M. Hossain, J. Marian, Stress-dependent solute energetics in W–Re alloys from first-principles calculations, Acta Mater. 80 (2014) 107–117.
[64] L. Gharaee, J. Marian, P. Erhart, The role of interstitial binding in radiation induced segregation in W-Re alloys, J. Appl. Phys. 120 (2) (2016) 025901.
[65] S. Giusepponi, M. Celino, The effects of vacancies in the mechanical properties of tungsten: a first-principles study, Nucl. Instrum. Methods Phys. Res., Sect. B 342 (2015) 70–75.
[66] W. Setyawan, G. Nandipati, R.J. Kurtz, Ab initio study of interstitial cluster interaction with Re, Os, and Ta in W, J. Nucl. Mater. 484 (2017) 30–41.
[67] L. Romaner, C. Ambrosch-Draxl, R. Pippan, Effect of rhenium on the dislocation core structure in tungsten, Phys. Rev. Lett. 104 (19) (2010) 195503.
[68] H. Li, S. Wurster, C. Motz, L. Romaner, C. Ambrosch-Draxl, R. Pippan, Dislocation-core symmetry and slip planes in tungsten alloys: ab initio calculations and microcantilever bending experiments, Acta Mater. 60 (2) (2012) 748–758.
[69] X. Wu, Y.-W. You, X.-S. Kong, J.-L. Chen, G.-N. Luo, G.-H. Lu, C. Liu, Z. Wang, First-principles determination of grain boundary strengthening in tungsten: dependence on grain boundary structure and metallic radius of solute, Acta Mater. 120 (2016) 315–326.
[70] U. Fischer, C. Bachmann, J.P. Catalan, T. Eade, D. Flammini, M. Gilbert, J. Jaboulay, A. Konobeev, D. Leichtle, L. Lu, F. Malouch, F. Moro, P. Pereslavtsev, Y. Qiu, J. Sanz, P. Sauvan, G. Stankunas, A. Travleev, A. Turner, F. Ogando, I. Palermo, R. Villari, Methodological approach for DEMO neutronics in the European PPPT programme: tools, data and analyses, Fusion Eng. Des. 123 (2017) 26–31.
[71] M.R. Gilbert, T. Eade, C. Bachmann, U. Fischer, N.P. Taylor, Waste assessment of European demo fusion reactor designs, Fusion Eng. Des. 136 (2018) 42–48.
[72] G. Federici, R. Kemp, D. Ward, C. Bachmann, T. Franke, S. Gonzalez, C. Lowry, M. Gadomska, J. Harman, B. Meszaros, C. Morlock, F. Romanelli, R. Wenninger, Overview of eu demo design and R&D activities, Fusion Eng. Des. 89 (7) (2014) 882–889. Proceedings of the 11th International Symposium on Fusion Nuclear Technology-11 (ISFNT-11) Barcelona, Spain, 15-20 September, 2013
[73] G. Federici, C. Bachmann, L. Barucca, W. Biel, L. Boccaccini, R. Brown, C. Bustreo, S. Ciattaglia, F. Cismondi, M. Coleman, V. Corato, C. Day, E. Diegele, U. Fischer, T. Franke, C. Gliss, A. Ibarra, R. Kembleton, A. Loving, F. Maviglia, B. Meszaros, G. Pintsuk, N. Taylor, M. Tran, C. Vorpahl, R. Wenninger, J. You, Demo design activity in Europe: progress and updates, Fusion Eng. Des. 136 (2018) 729–741. Special Issue: Proceedings of the 13th International Symposium on Fusion Nuclear Technology (ISFNT-13)
[74] Y. Qian, M.R. Gilbert, L. Dezerald, D. Cereceda, Using first-principles calculations to predict the mechanical properties of transmuting tungsten under first wall fusion power-plant conditions, J. Phys. 33 (34) (2021) 345901.
[75] M. Gilbert, J.-C. Sublet, Neutron-induced transmutation effects in W and W-alloys in a fusion environment, Nucl. Fusion 51 (4) (2011) 043005, doi:10.1088/0029-5515/51/4/043005.
[76] M. Gilbert, J.-C. Sublet, S. Dudarev, Spatial heterogeneity of tungsten transmutation in a fusion device, Nucl. Fusion 57 (4) (2017) 044002, doi:10.1088/1741-4326/aa5e2e.
[77] D. Sobieraj, J.S. Wróbel, T. Rygier, K.J. Kurzydłowski, O. El Atwani, A. Devaraj, E.M. Saez, D. Nguyen-Manh, Chemical short-range order in derivative Cr–Ta–Ti–V–W high entropy alloys from the first-principles thermodynamic study, Phys. Chem. Chem. Phys. 22 (41) (2020) 23929–23951.
[78] P. Giannozzi, S. Baroni, N. Bonini, M. Calandra, R. Car, C. Cavazzoni, D. Ceresoli, G.L. Chiarotti, M. Cococcioni, I. Dabo, et al., Quantum espresso: a modular and open-source software project for quantum simulations of materials, J. Phys. 21 (39) (2009) 395502.
[79] P. Giannozzi, O. Andreussi, T. Brumme, O. Bunau, M.B. Nardelli, M. Calandra, R. Car, C. Cavazzoni, D. Ceresoli, M. Cococcioni, et al., Advanced capabilities for materials modelling with quantum espresso, J. Phys. 29 (46) (2017) 465901.
[80] J.P. Perdew, K. Burke, M. Ernzerhof, Generalized gradient approximation made simple, Phys. Rev. Lett. 77 (18) (1996) 3865.
[81] L. Bellaiche, D. Vanderbilt, Virtual crystal approximation revisited: application to dielectric and piezoelectric properties of perovskites, Phys. Rev. B 61 (12) (2000) 7877.
[82] L. Romaner, V. Razumovskiy, R. Pippan, Core polarity of screw dislocations in Fe–Co alloys, Philos. Mag. Lett. 94 (6) (2014) 334–341.
[83] D. Hamann, Optimized norm-conserving vanderbilt pseudopotentials, Phys. Rev. B 88 (8) (2013) 085117.
[84] A. Handbook, Alloy phase diagrams, vol 03. ASM International, Materials Park, p. 556 and 1107 (1992).
[85] H.J. Monkhorst, J.D. Pack, Special points for brillouin-zone integrations, Phys. Rev. B 13 (12) (1976) 5188.
[86] A.J. Koning, D. Rochman, TENDL-2017, 2017, Release Date: April 25, 2018. Available from https://tendl.web.psi.ch/tendl_2017/tendl2017.html.
[87] M.R. Gilbert, J.-Ch. Sublet, Experimental decay-heat simulation-benchmark for 14 MeV neutrons & complex inventory analysis with FISPACT-II, Nucl. Fusion 59 (8) (2019) 086045, doi:10.1088/1741-4326/ab278a.
[88] M.R. Gilbert, J.-Ch. Sublet, Fusion Decay Heat Validation, FISPACT-II & TENDL-2017, EAF2010, ENDF/B-VIII.0, JEFF-3.3, and IRDFF-1.05 Nuclear Data Libraries, Technical report, UKAEA, 2018. Available from http://fispact.ukaea.uk
[89] F.H. Featherston, J. Neighbours, Elastic constants of tantalum, tungsten, and molybdenum, Phys. Rev. 130 (4) (1963) 1324.
[90] D. Jiang, S. Li, K. He, W. Hu, H. Wan, S. Liu, Excellent high temperature elasticity and thermodynamic properties of W-Cr alloys: a first-principles study, Nucl. Mater. Energy 34 (2023) 101367.
[91] Y. Ma, Q.-F. Han, Z.-Y. Zhou, Y.-L. Liu, First-principles investigation on mechanical behaviors of W–Cr/Ti binary alloys, J. Nucl. Mater. 468 (2016) 105–112.
[92] J. Veverka, F. Lukáč, A.P. Kądzielawa, M. Koller, Z. Chlup, H. Hadraba, M. Karlík, D. Legut, J. Vontorová, T. Chráska, et al., Ultrafine-grained W-Cr composite prepared by controlled W-Cr solid solution decomposition, Mater. Lett. 304 (2021) 130728.
[93] S. Zheng, S. Wang, First-principles design of refractory high entropy alloy VMoNbTaW, Entropy 20 (12) (2018) 965.
[94] S.-m. Zheng, W.-q. Feng, S.-q. Wang, Elastic properties of high entropy alloys by MaxEnt approach, Comput. Mater. Sci 142 (2018) 332–337.
[95] H. Yao, J. Qiao, J. Hawk, H. Zhou, M. Chen, M. Gao, Mechanical properties of refractory high-entropy alloys: experiments and modeling, J. Alloys Compd. 696 (2017) 1139–1150.
[96] H. Khakurel, M. Taufique, A. Roy, G. Balasubramanian, G. Ouyang, J. Cui, D.D. Johnson, R. Devanathan, Machine learning assisted prediction of the Youngs modulus of compositionally complex alloys, Sci. Rep. 11 (1) (2021) 17149.
[97] E. Fazakas, V. Zadorozhnyy, L. Varga, A. Inoue, D. Louzguine-Luzgin, F. Tian, L. Vitos, Experimental and theoretical study of Ti20Zr20Hf20Nb20X20 (X = V or Cr) refractory high-entropy alloys, Int. J. Refract. Met. Hard Mater. 47 (2014) 131–138.
[98] A. Roy, T. Babuska, B. Krick, G. Balasubramanian, Machine learned feature identification for predicting phase and Young's modulus of low-, medium-and high-entropy alloys, Scr. Mater. 185 (2020) 152–158.
[99] H. Cui, N. Liu, R. Zhou, D. Li, J. Cheng, First-principles study on the structures and elastic properties of W-Ta-V ternary alloys, Comput. Mater. Sci 202 (2022) 110940.

[100] M. Muzyk, D. Nguyen-Manh, K. Kurzydłowski, N. Baluc, S. Dudarev, Phase stability, point defects, and elastic properties of wv and w-ta alloys, Phys. Rev. B 84 (10) (2011) 104115.
[101] D. Nguyen-Manh, M.J. Cawkwell, R. Groger, M. Mrovec, R. Porizek, D.G. Pettifor, V. Vitek, Dislocation in materials with mixed covalent and metallic bonding, Mater. Sci. Eng., A 400–401 (2005) 68–71.
[102] M. Mrovec, R. Grger, A.G. Bailey, D. Nguyen-Manh, C. Elssser, V. Vitek, Bond-order potential for simulations of extended defects in tungsten, Phys. Rev. B 75 (2007) 104119.
[103] D. Cereceda, A. Stukowski, M. Gilbert, S. Queyreau, L. Ventelon, M. Marinica, J. Perlado, J. Marian, Assessment of interatomic potentials for atomistic analysis of static and dynamic properties of screw dislocations in W, J. Phys. 25 (8) (2013) 085702.
[104] Y.-H. Li, H.-B. Zhou, L. Liang, N. Gao, H. Deng, F. Gao, G. Lu, G.-H. Lu, Transition from ductilizing to hardening in tungsten: the dependence on rhenium distribution, Acta Mater. 181 (2019) 110–123.
[105] G. Bonny, D. Terentyev, A. Bakaev, P. Grigorev, D. Van Neck, Many-body central force potentials for tungsten, Model. Simul. Mater. Sci. Eng. 22 (5) (2014) 053001.
[106] G.D. Samolyuk, Y.N. Osetsky, R.E. Stoller, The influence of transition metal solutes on the dislocation core structure and values of the peierls stress and barrier in tungsten, J. Phys. 25 (2) (2012) 025403.
[107] J.R. Rice, Dislocation nucleation from a crack tip: an analysis based on the peierls concept, J. Mech. Phys. Solids 40 (2) (1992) 239–271.
[108] R. Ayres, G. Shannette, D. Stein, Elastic constants of tungsten- rhenium alloys from 77 to 298 K, J. Appl. Phys. 46 (4) (1975) 1526–1530.
[109] A. Koning, Bayesian Monte Carlo method for nuclear data evaluation, Nucl. Data Sheets 123 (2015) 207–213, doi:10.1016/j.nds.2014.12.036. Special Issue on International Workshop on Nuclear Data Covariances April 28 - May 1, 2014, Santa Fe, New Mexico, USA http://t2.lanl.gov/cw2014
[110] A. Koning, D. Rochman, J.-C. Sublet, N. Dzysiuk, M. Fleming, S. van der Marck, Tendl: complete nuclear data library for innovative nuclear science and technology, Nucl. Data Sheets 155 (2019) 1–55, doi:10.1016/j.nds.2019.01.002. Special Issue on Nuclear Reaction Data
[111] D. Wang, C. Wang, T. Yu, Effects of Re, W and Co on dislocation nucleation at the crack tip in the $\gamma$-phase of Ni-based single-crystal superalloys by atomistic simulation, R. Soc. Open Sci. 6 (7) (2019) 190441.
[112] Z.-G. Liu, C.-Y. Wang, T. Yu, Influence of Re on the propagation of a Ni/Ni3 Al interface crack by molecular dynamics simulation, Model. Simul. Mater. Sci. Eng. 21 (4) (2013) 045009.
[113] S. Shi, L. Zhu, H. Zhang, Z. Sun, R. Ahuja, Mapping the relationship among composition, stacking fault energy and ductility in Nb alloys: a first-principles study, Acta Mater. 144 (2018) 853–861.
[114] F. Hofmann, D.M. Mason, J.K. Eliason, A.A. Maznev, K.A. Nelson, S.L. Dudarev, Non-contact measurement of thermal diffusivity in ion-implanted nuclear materials, Sci. Rep. 5 (2015) 16042, doi:10.1038/srep16042.
[115] B. Kos, A. ufar, I.A. Kodeli, Asusd nuclear data sensitivity and uncertainty program package: validation on fusion and fission benchmark experiments, Nucl. Eng. Technol. 53 (7) (2021) 2151–2161, doi:10.1016/j.net.2021.01.034. https://www.sciencedirect.com/science/article/pii/S1738573321000553.
[116] Y. Hu, L. Bai, Y. Tong, D. Deng, X. Liang, J. Zhang, Y. Li, Y. Chen, First-principle calculation investigation of NbMoTaWbased refractory high entropy alloys, J. Alloys Compd. 827 (2020) 153963.
[117] L. Vitos, A. Ruban, H.L. Skriver, J. Kollár, The surface energy of metals, Surf. Sci. 411 (1–2) (1998) 186–202.
[118] B. Bienvenu, C.C. Fu, E. Clouet, Impact of magnetism on screw dislocations in body-centered cubic chromium, Acta Mater. 200 (2020) 570–580.
[119] J. Wang, S.-Q. Wang, Surface energy and work function of fcc and bcc crystals: density functional study, Surf. Sci. 630 (2014) 216–224.
[120] X. Wang, S. Xu, W.-R. Jian, X.-G. Li, Y. Su, I.J. Beyerlein, Generalized stacking fault energies and peierls stresses in refractory body-centered cubic metals from machine learning-based interatomic potentials, Comput. Mater. Sci. 192 (2021) 110364.
[121] X. Zhang, J. Tang, L. Deng, G. Zhong, X. Liu, Y. Li, H. Deng, W. Hu, The effects of interstitial impurities on the mechanical properties of vanadium alloys: a first-principles study, J. Alloys Compd. 701 (2017) 975–980.
[122] X.-J. Yao, X.-F. Shi, Y.-P. Wang, G.-Y. Gan, B.-Y. Tang, The mechanical properties of high entropy (-like) alloy $W_x(TaTiVCr)_{1-x}$ via first-principles calculations, Fusion Eng. Des. 137 (2018) 35–42.